Eocene-Oligocene large-scale circulation of the East Asian summer monsoon recorded in neritic carbonates of the proto-South China Sea

François Fournier, Thomas Teillet, Alexis Licht, Jean Borgomano, Lucien F. Montaggioni

Eocene-Oligocene large-scale circulation of the East Asian summer monsoon recorded in neritic carbonates of the proto-South China Sea

François Fournier *[1], Thomas Teillet [1,2], Alexis Licht [1], Jean Borgomano [1], Lucien Montaggioni [1]

[1] Aix Marseille Univ, CNRS, IRD, Coll France, CEREGE, Technopôle de l'Arbois-Méditerranée, BP80, 13545 Aix-en-Provence, France.

[2] King Abdullah University of Science and Technology (KAUST), Ali I. Al-Naimi Petroleum Engineering Research Center (ANPERC), Saudi Arabia

* *corresponding author:* fournier@cerege.fr

Abstract

When the modern features of large-scale Asian monsoonal circulation were set-up is poorly constrained and pre-Neogene monsoonal archives are rare. This study investigates the temporal evolution of neritic carbonates in the proto-South China Sea to reconstruct East Asian monsoonal currents and winds during the middle to late Paleogene. Analysis of three-dimensional seismic and well core data from the North-West Palawan block reveals the occurrence of a set of thick (>125 m), aggrading *Halimeda* bioherms, early Oligocene in age. By analogy with Holocene green algal buildup counterparts, they are interpreted to form in nutrient-rich areas subject to upwelling currents and reflect the early presence of a strong coastal jet in the Proto-South China Sea, as seen today during the summer monsoonal season. The analysis of the underlying mixed carbonate–siliciclastic ramp shows that mesotrophic conditions already prevailed during the late Eocene, thus suggesting that modern-like summer East Asian Monsoon large-scale circulation was possibly active as early as the late Eocene in the Proto-South China Sea. Evidence for

upwelling currents vanishes in late early Oligocene carbonate-producing biota, that are characterized by the significant development of euphotic hermatypic coral communities reflecting lower nutrient concentrations. This turnover coincides with the opening of the modern South China Sea and is interpreted to result from the southward drift of the North-West Palawan block which placed the area away from the Chinese margin and the coastal jet. Our results highlight therefore that many of the features of the summer East Asian Monsoon large-scale circulation are rooted in the middle Paleogene.

Keywords: monsoon, carbonates, Paleogene, Southeast Asia, *Halimeda*, coastal jet.

1. Introduction

Carbonate-producing biota are sensitive to many environmental factors including water temperature, light penetration, nutrient concentration, water chemistry, nature of substrate, stratification and circulation patterns within the water column and hydrodynamic regime (e.g. Hallock and Schlager, 1986; Mutti and Hallock, 2003). These factors are primarily controlled by global climate and geodynamics and operate at different time and space scales. For that reason, qualitative and quantitative variations in neritic carbonate production have proven to be excellent records of paleoclimatic and paleoceanographic changes during the Cenozoic in the Indo-Pacific realm (e.g. Mathew et al., 2020), the Caribbean (Reijmer et al., 2002) and the Mediterranean (Cornacchia et al., 2021). In the Indian Ocean, they are influenced by the large-scale monsoonal circulation and document the evolution of the South Asian Monsoon on geological time scales (Betzler et al., 2009).

Like the South Asian Monsoon, the East Asian Monsoon (EAM) is associated with a large-scale circulation that supplies moisture from the Sunda seas, the Pacific, and the South China

Sea (SCS) to East Asia in summer. This summer circulation is characterized by strong southerly winds over the SCS, which are amplified by Sundaland topography and form a southwesterly coastal jet offshore Vietnam (Xie et al., 2003) (**Fig. 1A**). The coastal jet generates a well-marked upwelling zone in the SCS (Dippner et al., 2007), activity of which has been tracked as early as the early Miocene in heterozoan carbonate systems (Wu et al., 2019). Earlier records of EAM large-scale circulation are rare: on land, paleovegetation reconstructions suggest the presence of a summer, monsoon-like rainy season since at least the middle Eocene (Quan *et al.*, 2012; Licht *et al*., 2014; Spicer et al., 2016; Sorrel *et al*., 2017). This proto-monsoonal regime has been either attributed to the seasonal migration of the intertropical convergence zone (ITCZ; Spicer et al., 2016; Farnsworth et al., 2019) or a weak sea-breeze circulation (Tardif et al., 2020). Other authors argued for a major stage of wettening in the Late Eocene, around 36 Ma (Zheng *et al*., 2022).

The study of the Paleogene carbonate systems in the proto-SCS, before the opening of the modern SCS starting in the middle Oligocene (Briais et al., 1993; Li et al., 2014), enables to reconstruct past upwellings and provide insights into potential large-scale monsoonal circulation. They thus provide a key approach to elucidate early EAM dynamics. Hydrocarbon exploration boreholes and seismic acquisition performed on the North Palawan Block (Malampaya Field) (**Fig. 1B**), revealed the occurrence of Early Oligocene algal-dominated, aggrading carbonate buildups overlying a Upper Eocene mixed carbonate-siliciclastic ramp (Fournier et al., 2005). The present paper aims at 1) characterizing changes in carbonate producing biota during the Late Eocene and Early Oligocene, 2) interpreting the carbonate factories in terms of paleoceanographic settings and upwelling dynamics based on sedimentologic and paleoecological analysis of cores and comparison with modern analogues, and 3) drawing implications on the paleoceanographic evolution of the proto-SCS and early EAM.

2. Geological setting

The SCS is the largest marginal sea of the western Pacific region and results from rifting and seafloor spreading along the South China margin (**Fig. 1**). The SCS was preceded by the Paleogene proto-SCS, a sea of similar amplitude bracketed between the Chinese margin and Borneo (Zhou et al., 1995; Hall, 2002; Morley, 2016). Slab-pull effects related to subduction of the proto-SCS beneath north-west Borneo resulted in early to middle Paleogene rifting along the South China margin and separation of the Calamian–North Palawan–North Borneo micro-continent (CPBC; Hall, 2002). Oceanic sea floor spreading initiated at ca 32-31 Ma and resulted in the southward drift of the CPBC and the opening of the modern SCS between the Chinese margin and the CPBC (Briais et al., 1993; Hutchison et al., 2000; Clift et al., 2008; Li et al., 2014). During the Early-Middle Miocene, the CPBC collided with the accretion wedge of the Paleogene subduction zone of Borneo-North Cagayan, marking the final disappearance of the proto-SCS and causing the end of SCS seafloor spreading (dated at ca. 15 Ma; Briais et al., 1993; Li et al., 2014). There is little evidence for Eocene-earliest Oligocene syn-rift carbonate sedimentation (Fournier et al., 2005), but widespread carbonate platforms are recorded in upper Oligocene and lower Miocene deposits on both the northern (e.g. Wu et al., 2019; Mathew, 2020) and southern margins of the SCS (Malampaya, North Palawan basin: Fournier et al., 2005; Reed Bank: Ding et al., 2015; Dangerous Ground: Steuer et al., 2014). Carbonate platforms from the North Palawan block were drowned during the Middle Miocene because of increased subsidence, down-warping of the northwestern part of the block and important clastic supply from the uplifted Palawan Island (Fulthorpe and Schlanger, 1989). Older Paleogene carbonate systems can be found on the CPBC and are associated with the northern margin of the proto-SCS (Fournier et al., 2005).

Our study area, the gas and oil field of Malampaya (**Fig. 2**), is located in the deep-water (850 m to 1200 m) block SC 38 in offshore Palawan on the North Palawan Block (part of the CPBC). Located 3000 m below the modern sea level, this late Eocene to early Miocene carbonate buildup consists of a 5 km long, 1-2 km wide, and 600 m thick NE-SW oriented body. Previous works on the Malampaya buildups focused on the Nido Limestone reservoir (late Rupelian to Burdigalian); it is made of aggrading, cyclic shallow-water carbonate units dominated by seagrass-related foraminifers, red algae and corals (Fournier et al., 2004; 2005) and punctated by repeated subaerial exposures (Fournier et al., 2004; 2007). Syn-depositional tectonic deformation of the Nido Limestone has been shown to control carbonate accumulation and preservation on top of the buildup (Fournier et al., 2005). There is so far no detailed petrographic and sedimentological investigation of the pre-Nido (Eocene-early Rupelian) carbonates.

3. Database and methods

The data set consists of a 3-D seismic survey acquired by Shell Philippines in 2002 and well data from three wells (MA-1, MA-2 and MA-5) having reached the Eocene and Early Oligocene carbonates. The non-SEG seismic polarity convention has been used (negative amplitude means positive reflection coefficient). The well-to-seismic tie used in this study is that of Fournier and Borgomano (2007). The correspondence between sedimentary units and the main seismic horizons from the Eocene-Lower Oligocene interval is reported in **Fig. 3**. The interpretation of the base of carbonates (BN horizon) and top of the Early Oligocene algal buildups (R20.1 horizon) has been revised in the present work. The chronostratigraphic framework of the Malampaya buildup is based on the letter stage classification, a large benthic foraminifera biozonation (Adams, 1970; Renema, 2007). Key foraminiferal taxa used for the

biostratigraphic analysis and corresponding letter stages are reported in **Fig. 4B**. In contrast to previous works (Fournier et al., 2004), the base of Lower Te stage (**Fig. 4B**) has been defined by the last downhole occurrence of *Heterostegina* (*Vlerkina*) *borneensis* instead of that of the rotaliid *Neorotalia mecatepecensis* which has been reported from Rupelian (Td) limestones in Java (Lunt and Renema, 2014).

A total of 42 thin-sections from the Eocene-Early Oligocene interval has been prepared from core and side-wall samples (in wells MA-1 and MA-2) as well as from cuttings (in well MA-5) and analyzed for detailed petrographic characterization using a conventional transmitted polarized light microscope. Quantitative analysis of the biota has been performed by point-counting (300 points) using *JMicroVision* software.

4. Results

4.1. Chronostratigraphic framework and well-correlation

The base of the carbonate succession is late Eocene in age (Tb letter stage after Adams, 1970; Renema, 2007) in wells MA-1, MA-2 and MA-5 (**Fig. 4** and **Fig. 5**), based on the co-occurrence of *Pellatispira* and *Discocyclina*. Rupelian deposits (Tc-Td letter stage) have been identified within an up to 85 meter-thick interval, on the basis of the occurrence of *Nummulites*, *Halkyardia* and *Borelis pygmaeus* together with the lack of strictly pre-Oligocene taxa such as *Discocyclina* and *Pellatispira*. The presence of *Cycloclypeus* in the upper part of the Rupelian interval in MA-2 (**Fig. 4**), allows characterizing the late Rupelian (Td stage). The base of Chattian deposits has been defined as representing the last downhole occurrence of *Heterostegina borneensis*. The Eocene-Oligocene carbonate succession was subdivided by Fournier and Borgomano (2007) into 6 depositional units (SR1, SR2, SC1.1, SC1.2, SC2.1 and SC2.2). According to the revised biostratigraphic framework, SR1 is late Eocene in age (Tb),

SR2 would correspond to the early Rupelian (Tc) while SC1.1 is comprised entirely within the late Rupelian (Td). The base of Chattian deposits closely corresponds to SC1.2 unit which is characterized by repeated subaerial exposures (Fournier et al., 2004). Based on the revised chronostratigraphic framework and seismic horizon constraints, a well-correlation panel has been established between wells MA-1, MA-2 and MA-3 (**Fig.3**), showing the significant thickening of early Rupelian unit SR2 at well MA-2.

4.2. Seismic geomorphology of early Rupelian buildups

The 3D interpretation of Base Nido (BN), R10.1 (Top Eocene) and R20.1 (Top early Rupelian) reflectors reveals the occurrence of four main high-relief buildups (Buildups A, B,C,D: **Fig. 6** and **7**), corresponding to the SR1 unit, whose basal diameter ranges from 800 to 1300 meters and a set of adjacent smaller buildups. Buildups B,C, D are nearly conical in shape while buildup A exhibits a flattened top. Around well MA-2, internal reflectors within Buildup A are mound-shaped and display downlap terminations onto Top Eocene reflectors. Similar downlap terminations are present within buildups B and C (**Fig. 6** and **7**) but internal reflectors exhibit apparent steeper slopes and locally a more chaotic expression. Below buildups A, B, C and D, Top Eocene and Base Nido reflectors are crosscut by nearly vertical faults thus suggesting that buildups developed on crests of tilted blocks (buildups B,C,D: **Fig. 7**) or on horst structure (Buildup A: **Fig. 6**). The western flank of Buildup A is onlapped by top Rupelian (C11.1) reflector while the eastern flank is onlapped by low amplitude reflectors from the Miocene Pagasa siliciclastics **(Fig. 2D-E**). Buildups B, C and D are overlain by westward dipping Pagasa deposits. The westernmost buildup (Buildup A) has been penetrated by well MA-2, thus making possible the quantification of dimensions, thickness and slope dips of such carbonate bodies and enabling the determination of the nature of carbonate producers. The interval velocity (**Supplementary Material S1**) of early Rupelian unit (SR2) calculated from well-to-seismic

tie results (5040 m/s) is very consistent with the value computed from the integration of sonic log (5070 m/s). Based on computed interval velocity (5040 m/s) and two-way-time thicknesses measured from seismic data, the maximum thickness of early Rupelian buildups has been estimated to range from 125 m (Buildup A) to 580 m (Buildup C). Estimated dip angles of buildup flanks range from 21° (Buildup A) to 42° (Buildup C). Quantified morphological parameters for buildups A, B, C and D are displayed in **Table 1**.

4.3. Late Eocene and Early Oligocene depositional facies and facies associations

The nature of the carbonate producers leading to the construction of the aggradating carbonate buildups revealed by 3D seismic interpretation (**Fig. 6** & **7**) has been determined by means of a detailed petrographic analysis of the cores and thin sections from well MA-2, located in the upper part of the Buildup A southern flank. The underlying Upper Eocene carbonates have been investigated from the analysis of cores, side-wall samples and cuttings from wells MA-1, MA-2 and MA-5. Grain composition of analysed samples is summarized in **Supplementary Material S2** and average composition is displayed in **Fig. 8**.

4.3.1. Late Eocene Facies Association (EFA): quartz-rich bryozan, foraminiferal, coralline algal limestones

In spite of a relative homogeneity in bioclastic composition, two depositional facies have been identified within the late Eocene interval in wells MA-1, MA-2 and MA-5 (**Fig. 3**), based essentially on distinct depositional texture and quartz grain content.

Facies FE1: Quartz-rich, foraminiferal-coralline algal grainstone

FE1 facies, identified in the lower part of the Upper Eocene interval in wells MA-1, MA-2 and MA-5 (**Fig. 3**), consists of a foraminiferal-coralline algal grainstone with significant proportions (average: 27%) of angular to sub-angular, fine to medium-grained quartz particles (**Fig. 8 & 9A-B**). Large benthic foraminifers (27% of grains in average) dominate the biotic assemblage together with fragments of encrusting coralline algae (24%). The foraminiferal assemblage is dominated by lense to flat-shaped *Discocyclina* and *Pellatispira*, commonly displaying broken edge. *Nummulites* and miliolids are scarce. Subordinate components are bryozoans (13%) and echinoderms (5%). The intergranular space is entirely occluded by coarse sparry calcite cements.

Facies FE2: Quartz-bearing, bryozoan, foraminiferal, coralline algal packstone

Facies FA2 is a quartz-bearing (10% of the grain content in average) packstone (**Fig. 8 & 9C-D**) whose biota is dominated by bryozoan (28%), encrusting coralline algae (27%) and large benthic foraminifers (26%) with minor proportions of echinoderms (5%). Quartz particles are typically fine-grained and angular. Similarly to FE1, the foraminiferal assemblage is dominated by *Discocyclina* and *Pellatispira* together with scarce *Nummulites,* agglutinated foraminifers and miliolids.

4.3.2. Early Rupelian Facies Association (ERFA): Halimeda-coralline algal-foraminiferal limestones

Facies FR1: *Halimeda* floastone-rudstone

Facies FR1 consists of a *Halimeda* rudstone or *Halimeda* floatstone with a coralline algal-foraminiferal grainstone matrix (**Fig. 10A-D**). Sediment is dominated (from 30 to 66% of the

grain fraction; average: 42%: **Fig. 8**) by 3–8mm-long segments of rarely broken *Halimeda* segments . Typically, the segments are chaotically jumbled, sometimes vertically-oriented (**Fig. 10A-D**), thus forming large (mm-scale) and irregular shelter cavities. Encrusting coralline algae are the main skeletal grain forming the grainstone matrix (26% in average of the whole skeletal fraction) and are preserved as medium-grained fragments. Articulated coralline algae are also present (5%). The foraminiferal assemblage is dominated by porcelaneous forms (10% in average of the whole skeletal fraction) including miliolids, alveolinids (*Borelis pygmaeus*), soritids and peneroplids. Hyaline forms are scarcer and mainly consist of lense-shaped to flat *Nummulites*. Corals are uncommon (0.25% in average) and preserved as small fragments of branching colonies. The intergranular space may be partially, geopetally filled by peloidal micrite (**Fig. 10A & D**) and the residual pore space may be preserved or occluded by various generations of sparry calcite cements. The occurrence of lime mud sediment postdating perigranular calcite cements in sheltered cavities (**Fig. 10A**) strongly suggest very early, syn-depositional cementation of the sediment.

Facies FR2: Coralline algal-foraminiferal-*Halimeda* packstone

Facies FR2 is a coralline algal-foraminiferal packstone encasing sparse and well preserved *Halimeda* thalli (**Fig. 10 E-F**). FR2 is present as meter-thick beds, intercalated within FR1. Encrusting coralline algae are the dominant skeletal component (41% in average: **Fig. 8**) while benthic foraminifers and *Halimeda* represent respectively 26% and 14% of the grain fraction. Echinoderms are a subordinate but significant skeletal component (6%). The foraminiferal assemblage is composed of flat-shaped *Nummulites* and *Amphistegina*, together with textulariids, miliolids and few planktonics. Pteropods (**Fig. 10E**) and solitary coral (**Fig. 10F**) are occasionnaly present.

Facies FR3: Rhodolitic floatstone

Facies FR3 has been reported only at the base of the early Rupelian interval and forms a 3-meter-thick interval of rhodolithic floatstone which is made of lumpy to fructicose rhodoliths, up to 5 cm in diameter, embedded within a foraminiferal-*Halimeda* packstone (**Fig. 10G**). Rhodoliths represent the dominant skeletal component (46%), while benthic foraminifers and *Halimeda* represent respectively 17% and 28% of the grain fraction (**Fig. 8**). In contrast to facies FR1 and FR2, *Halimeda* thalli are generally broken as well as most of the foraminiferal tests. The foraminiferal assemblage is composed of operculinids, *Amphistegina*, miliolids, alveolinids together with scarce planktonics.

5. DISCUSSION

5.1. Late Eocene mixed carbonate-siliciclastic ramp: a record of syn-rift transgression

The quartz-rich foraminiferal- coralline algal grainstone (FE1 facies) sampled in the lower part of the late Eocene interval from the three analyzed wells contain abundant robust *Discocyclina* thus suggesting shallow, tropical, agitated, open marine waters in inner ramp setting (Sinclair et al., 1998). The lack of matrix mud as well as the broken edges of foraminiferal tests in facies FE1 support also a high energy setting. The other dominant foraminiferal taxa, *Pellatispira*, is known to preferentially thrive in the lower part of the upper photic zone and the upper part of the lower photic zone (Romero et al.,2002), such a bathymetric interval being equivalent with the mesophotic zone and upper oligophotic zone of Pomar (2001). The association of oligo-

mesophotic biota and high-energy markers consistent with a deposition above the fair-weather wave-base (<20 m) may suggest: 1) turbid water conditions since decreased light penetration rates induce a shift of the mesophotic zone toward shallower location (e.g. Pomar et al., 2014), or 2) the occurrence of internal waves breaking obliquely to the sloping ramp (Pomar et al., 2012). Additionnally, large benthic foraminifers such as *Discocyclina* and *Pellatispira* have a mixotrophic nutrition, which favours their development in low-nutrient conditions, and therefore they preferably thrive in oligotrophic habitats (e.g. Mutti and Hallock, 2003, Hallock and Pomar, 2009).

In FE2, the foraminiferal association is similar to that of FE1 but the facies differs in displaying a lime mud matrix, a higher content in bryozoan and finer-grained quartz sand particles. The presence of matrix mud is indicative of low-energy environments, the abundance of bryozoan is likely to represent low-light and nutrient-rich environments and the decreased quartz sand size may suggest a more distal location relatively to terrigenous supplies. Fine-sized quartz grains can be explained by the input of suspended particle supply from erosion of the hinterland (the crest of the Malampaya tilted block: **Fig. 2B**). Facies FE2 likely occupy a slightly deeper position, below the fair-weather wave base, within a nutrient-enriched oligophotic environment. Robust large benthic foraminifera (*Discocyclina*) and fragments of coralline algae likely derive from shallower areas. The present results together with the analogy with other Eocene carbonate systems dominated by large benthic foraminifers and coralline algae (e.g. Romero et al. 2002; Khanolkar and Saraswati, 2019) suggest a carbonate ramp system, subject to terrigenous influxes and characterized by a mesophotic, oligotrophic, turbid-water, high-energy outer inner ramp to mid-ramp (FE1 facies) and an oligophotic, mesotrophic, low-energy outer ramp (FE2 facies). Additionnally, the vertical upward succession from FE1 to FE2 suggests that the late Eocene carbonate ramp (SR1 unit *sensu* Fournier and Borgomano, 2007) developed during a marine transgression over the Pre-Nido basement.

5.2. Depositional model for early Rupelian *Halimeda* buildups

Except the lowermost 2 meters of carbonate sediments overlying the late Eocene deposits (core 5) which are made of a rhodolithic floatstone (FR3: **Fig. 10G**), the carbonate succession crossed by MA-2 well consists essentially of *Halimeda* floatstone-rudstone (FR1) with thin (meter-thick) occurrences of foraminiferal-coralline algal packstones (FR2) (**Fig. 11**). In FR1 floatstones-rudstones, the peloidal and geopetal nature of the sediment infilling the large cavity formed by the chaotic accumulation of *Halimeda* segments, prior to mechanical compaction (**Fig. 10A-D**), suggests early (microbial?) carbonate precipitation leading to a syn-sedimentary lithification. Additionnally, the occurrence of peloidal micrite postdating isopacheous cements (**Fig. 10A**) suggests that early lithification occurred also by means of sparry calcite precipitation. The chaotic orientation and full preservation of *Halimeda* segments are indicative of rapid sediment accumulation resulting from prolific growth of *Halimeda* followed by spontaneous plant fragmentation and limited grain transport. Such a rapid *Halimeda* segment accretion coupled with syn-sedimentary cementation has been shown to result in reef structure development on the slopes of the early Messinian carbonate platform from the Sorbas Basin, Spain (Braga *et al*., 1996). The foraminiferal assemblage from FR1, with common miliolids and porcelaneous epibionts (soritids, *Borelis*) together with lense-to-flat shaped large benthic foraminifera suggest a relatively shallow-water environements (Hallock and Pomar, 2009; Pomar et al., 2014), at the transition between the euphotic and mesophotic zones. The scarcity of micrite particles (except in microbial peloids) in the intergranular space in most samples suggests a minimal water energy, sufficient to remove micron-scale particles. The *Halimeda* floatstone-rudstone likely deposited in a quiet-water environment with minimal wave energy near the fair-weather wave base, within the lower euphotic to upper mesophotic zone (~20 meters water-depth in waters of normal transparency). The aggrading nature of the early Rupelian buildups is likely to be related to the

fast accumulation of *Halimeda* segments and syn-sedimentary lithification, thus forming rigid *Halimeda* bioherms resisting to the effect of potential storms and limited the offbank export of sediments. The mud-supported FR2 facies, which is interbedded within FR1 *Halimeda* floatstones-rudstones may represent offbank sedimentation in a slightly deeper and low-energy environment or could be also related to a temporary deepening of the system considering some potential sea-level fluctuations. The foraminiferal assemblage with flat-shaped *Nummulites* and *Amphistegina* (Hallock and Pomar, 2009) suggests oligo-mesophotic environments. The occurrence of planktonic foraminifers and pteropods is also indicative or relatively deep and open marine environments. The presence of *Halimeda* plates in reduced proportions may suggest limited offbank transport from the neighbouring *Halimeda* bioherms. They may also derive from *in situ* fragmentation of sparse *Halimeda* plants growing on a muddy substrate in such oligo-mesophotic environment. In the rhodolithic floatstone FR3, the mud-supported fabric suggests a deposition below the fair-weather wave base. Rhodolith growth forms have been commonly assumed to be controlled by water energy levels and lumpy to fructicose rhodoliths are often associated with low to moderate energy environments (Bosence, 1983). The broken nature of most of *Halimeda* plates and foraminiferal tests suggests the occurrence of high energy events. The foraminiferal assemblage, similar to that of FR2 facies suggests oligo-mesophotic environments. Finally, the rhodolithic floatstone (FR3) may be interpreted as being deposited on the slopes of the buildups, in calm, oligo-mesophotic environments subject to episodic high energy events or may just represent an incipient stage of carbonate factory development (FE3) on some meso-oligophotic environment prior to the development of *Halimeda* meadows. The latter facies, captured in well MA-2 at the base of the buildup may represent at downslope lateral equivalent of FR2 facies, or may be restricted to specific hydrodynamic conditions prevailing during the incipient stages of buildup development.

5.3. Halimeda buildups development: a record of offshore upwelling

Seismic interpretation (**Fig. 6** & **7**) show that Halimeda buildups developed on bathymetric highs that are controlled by normal faults associated with rifting of the South China Sea. Increasing subsidence rate toward the southeast associated with block tilting (**Fig. 12**) is likely to be partly responsible for the greater thickness for buildups B, C and D (up to 220 ms TWT, ~580m) compared to buildup A (50 ms TWT, ~125m). These observations indicate that the location of early Oligocene *Halimeda* bioherms was partly driven by small changes of bathymetry controlled by the locus of extensional faults. However, these topographic highs do not fully explain the appearance of *Halimeda* bioherms in the early Oligocene, as many other carbonate systems such as coral reefs (e.g. Gishler and Hudson, 2004) can thrive on shallow bathymetric highs.

The distribution of Holocene and modern Halimeda bioherms is restricted to low energy marine tropical environments, with a range of water depth from 20 to 50 meters; they form mounds of up to 140 meters high (Mc Neil et al., 2020). They are today observable in five localities: 1) Kalukalukuang Bank, Eastern Java, Indonesia (Roberts et al., 1988), 2) Nicaraguan Rise, Miskito Channel, South-west Caribbean (Hine et al., 1988), 3) Northern Great Barrier Reef, Australia (e.g. Davies and Marshall, 1985; McNeil et al., 2020), 4) Swain Reefs, southern Great Barrier Reef, Australia (Searle and Flood, 1988), 5) Big Bank Shoals, Timor Sea (Heyward et al., 1997). Additional references are displayed in **Supplementary Material S3**. All of them are located coastward of deep-water upwelling zones: the Halimeda bioherms from the Kalukalukuang Bank are located in the southern Makassar Strait where upwelling occurs annually during southeast monsoon period (Utama et al., 2017); the mounds from the Miskito channel develop in nutrient rich-waters related to the upwelling of the ocean-scale Carribean Current impinging the steep margin of the Nicaragua shelf (Roberts et al., 1992); the Halimeda algal bioherms from the northern Great Barrier Reef are distributed within a N-S-oriented band located in mid-shelf to outer reef barrier position and appear to develop preferentially in areas where shelf-edge

upwelling from the Coral Sea intrudes into the shelf (McNeil et al., 2020); finally, Halimeda mounds from the southern Timor Sea occur in nutrient-rich waters subject to upwelling of water from the Indonesian throughflow during winter SE monsoon (Alongi et al., 2013).

The close association of *Halimeda* bioherms with upwelling zones is explained by the high concentrations in nutrients which favour the development of benthic frondose algae, including *Halimeda*, together with benthic suspension feeders (Hallock and Schlager, 1986; Hallock et al., 1988). The development of *Halimeda* buildups during the earliest Oligocene in Malampaya is therefore interpreted as resulting from high nutrient concentration on the northwest Palawan shelf and requires the set-up of an upwelling zone offshore in the Proto-SCS, in the absence of any alternate mechanism to explain high nutrient concentrations. These interpretations date the onset of upwelling offshore the Vietnamese coast back to at least the earliest Oligocene, before the sea-floor spreading of the SCS. The early Cenozoic paleogeographic history of the Palawan Continental Terrane (PCT), on which the studied carbonate systems are located, is controversial, particularly with regard to its pre-drift location along the South China margin (Morley, 2012; Zahirovik et al., 2014). Analyses of heavy mineral and detrital zircon U–Pb age signatures revealed that the PCT was attached to the South China margin from the Cretaceous until the Oligocene oceanization of the SCS (Shao et al., 2017). As a consequence, even though narrow (<50 km), marine troughs have developed during the Late Eocene to Early Oligocene rifting of the SCS, offshore southern China (Baiyung trough, Pearl River Basin: Sun et al., 2020), the PCT was open to the south-east to a wide oceanic basin (the Proto South China Sea) of comparable dimension (around 1500 km of width along a northwest-southeast transect) and orientation as the present-day SCS (**Fig. 1**).

5.4. Paleoclimatic and paleogeographic implications

393 The genetic link between the upwelling in the modern and Neogene SCS and the southwesterly
394 summer coastal jet offshore Vietnam (Xie et al., 2003; Dippner et al., 2007; Wu et al., 2019)
395 indicates that an early version of the coastal jet was active in the earliest Oligocene (**Fig 1 A &**
396 **B**). This jet is the coastal expression of the large-scale summer EAM circulation over the SCS
397 that carries atmospheric moisture from low-latitude oceanic pools to the eastern and northern
398 Chinese coast. Evidence for an active jet in the early Oligocene contrasts with the weak sea-
399 breeze model proposed for the late Eocene EAM, which does not involve a large-scale summer
400 circulation (Tardif et al., 2020). It remains unclear if a seasonal ITCZ migration over East Asia,
401 as proposed by several studies to explain monsoon-like rainfall in the Paleogene (Spicer et al.,
402 2016, Farnsworth et al., 2019), could seasonally generate such a jet. The modern Australian-
403 Indonesian monsoon, modern analogue for an ITCZ-driven monsoon (Spicer et al., 2016), is
404 driven by the seasonal migration of sea surface temperature maximum from one hemisphere to
405 the other and is associated with weaker and more gradual changes in wind direction and rainfall
406 than the EAM and South Asian monsoons (Wheeler and McBride, 2005). We thus postulate that
407 the early Oligocene jet of the proto-SCS better reflects the set-up of a modern-like EAM summer
408 large-scale circulation than an ITCZ-driven monsoon. Together with evidence for the Eocene
409 set-up of a modern-like winter EAM circulation based on dust records on land (Licht et al., 2016;
410 Meijer et al., 2021), our results suggest that many of the features of the summer and winter EAM
411 large-scale circulation are rooted in the middle Paleogene, which is also consistent with the
412 climate transition noted by Zheng et al. (2022) in Yunnan at 36 Ma..
413 The shift from a late Eocene carbonate ramp (facies FE1 and FE2) to a neritic environment
414 influenced by upwelling waters can first be interpreted as related to a strengthening of the EAM
415 summer circulation and associated jet. This interpretation is yet not straightforward, as inland
416 records indicate a decrease in EAM intensity through the Eocene-Oligocene Transition (Page et
417 al., 2019; Licht et al., 2020), caused by the minor yet significant dependency of the EAM

hydrological cycle to atmospheric pCO2 (Licht et al., 2014; Farnsworth et al., 2019). The 70 m eustatic drop in the earliest Oligocene resulted in the emergence of significant parts of the southeast Asian shelf, a process that increased land-sea thermal contrasts at the continental scale (Toumoulin et al., 2022). This mechanism can explain summer wind strengthening in the earliest Oligocene in a context of decreased moisture supply. However, the biological associations identified in the Late Eocene ramp reveal that nutrient concentrations increased distally: oligotrophic in the inner to middle ramp (Facies FE1) and mesotrophic in the outer ramp (facies FE2). This suggests that Eocene nutrients derived from ocean waters rather than from continental supply. We thus suggest that the upwelling in the proto-SCS (and the summer jet) possibly predated the earliest Oligocene, and that the apparent lack of *Halimeda* in the Eocene deposits is explained by other controlling factors.

A bathymetric control on the onset of algal buildups can be ruled out, as both late Eocene and early Oligocene carbonate facies suggest a shallow depth (<50 m) favorable to the development of *Halimeda* bioherms. Sea level drop associated with the Antarctic ice-sheet growth at the Eocene-Oligocene transition possibly resulted in the temporary emergence of our study area; this emergence could mark the top Eocene sequence boundary but left no evidence of subaerial exposure or shallowing trend in the sedimentary record. A decrease of terrigenous supply related to a regional drop of monsoonal intensity, reducing water turbidity and enhancing green algal productivity in the SCS, provides an alternate explanation for the appearance of *Halimeda* bioherms.

The disappearance of *Halimeda* build-ups and the shift to a carbonate sedimentation dominated by coralline algae, benthic foraminifers and corals in the late Rupelian Nido Limestone (SC1 units) is coeval to the initiation of oceanic sea floor spreading (ca 32-31 Ma) and the opening of the modern SCS between the south Chinese margin and the CPBC (Briais et al., 1993; Li et al., 2014). The opening of the modern SCS resulted in an increased southward drift of the CPBC,

443 away from the Chinese margin and the coastal jet. In the long-term, these changes must have
444 forced upwelling to jump north of the CPBC, in the modern SCS, which is achieved by the early
445 Miocene (Wu et al., 2019). The disappearance of *Halimeda* buildups on the North Palawan Block
446 (**Fig. 11** and **12**) in the late Rupelian can reflect a possible early jump of the upwelling from the
447 proto-SCS to the modern SCS. The late Oligocene and early Miocene carbonate production on
448 the North Palawan Block was dominated by seagrass related biota (**Fig. 12**) and characterized by
449 significant development of shallow euphotic hermatypic corals (Fournier et al., 2004) thus
450 indicating low to moderate nutrient concentrations. The period spanning from the late Rupelian
451 to the early Miocene was rather a transitory phase where the abyssal depths of the proto-SCS
452 were too far away from the coastal jet to be influenced by Ekman pumping and generate seasonal
453 upwellings, while the modern SCS, with its young and narrow oceanic crust, was too shallow for
454 upwellings to start. The disappearance of *Halimeda* build-ups is therefore interpreted to reflect a
455 possible shut-down of upwelling during the late Rupelian in response to this unfavorable
456 paleogeographic configuration.

457 ## 6. Conclusion

458 By coupling the interpretation of three-dimensional seismic data and drill cores, we show that
459 three different carbonate systems succeeded each other from the late Eocene to the late early
460 Oligocene offshore North-West Palawan. These results highlight two major turnovers in
461 carbonate production on the northern margin of the Proto-SCS and later on the southern margin
462 of the SCS, and provide insights into paleoclimatic and paleoceanographic changes in South-
463 East Asia from the Late Eocene to the Early Miocene:

464 -During the Late Eocene, a mixed carbonate-siliciclastic system was dominated by large benthic
465 foraminifers (*Discocyclina-Pellatispira* assemblage), coralline algae and bryozoan, developed
466 in nutrient-enriched and turbid waters. Nutrients were likely sourced by upwelling currents

prevailing in the Proto-SCS while turbidity was controlled by terrigenous supplies from the continent.

-During the Early Oligocene, terrigenous inputs ceased on the North Palawan Block and thick, aggrading *Halimeda* bioherms developed at water-depths ranging from 20 to 50 meters, as a result of the combination of high nutrient supplies sourced by upwelling currents, low-turbidity waters and tectonic subsidence.

-Such upwelling currents affecting the North Palawan Block are interpreted to reflect the onset of a coastal jet in the Proto-SCS which would have resulted from the set-up of a modern-like EAM summer large-scale circulation as early as the late Eocene.

- From the late early Oligocene to the early Miocene, the carbonate production on the North Palawan Block was characterized by significant development of shallow euphotic hermatypic coral communities which indicate a return to lower nutrient levels. Such a carbonate production turnover coincides with the opening of the modern SCS which resulted in a southward drift of the CPBC, away from the Chinese margin and the coastal jet.

This study shows the important and often underestimated potential of neritic carbonate systems and carbonate production turnovers to record major oceanographic changes such as those associated with monsoonal activity. Though our results do not address inland monsoonal circulation neither its low-latitude component, they emphasize the early origin of the offshore large-scale monsoonal circulation in East Asia, and contrast with the more recent, supposed age of the modern South Asian large-scale circulation over the Indian Ocean and the Arabian Sea, dated to the middle Miocene (Sarr et al., 2022).

Acknowledgements

Shell Philippines Exploration B.V. (SPEX) is acknowledged for supporting the PhD thesis (F. Fournier) on which the present work is based. We thank Anta Sarr for prolific discussions on monsoonal circulation.

References

Adams, C. G. (1970). A reconsideration of the East Indian Letter Classification of the Tertiary. Bulletins of the British Museum (Natural History), 19, 3, 87–137.

Alongi, D.M., Brinkman, R., Trott, L.A., da Silva, F., Pereira, F., Wagey, T. (2013). Enhanced benthic response to upwelling of the Indonesian Throughflow onto the southern shelf of Timor-Leste, Timor Sea. Journal of Geophysical Research: Biogeosciences, 118, 1-13.

Bosence, D. W. J. (1983). Decription and Classification of Rhodoliths (Rhodoids, Rhodolites). Coated Grains, C, 217–224.

Braga, J.C., Martín, J.M. and Riding, R. (1996) Internal structure of segment reefs: Halimeda algal mounds in the Mediterranean Miocene. Geology, 24, 35–38.

Boudagher-Fadel, M.K., Banner, F. (1999). Revision of the stratigraphic significance of

the Oligocene–Miocene “Letter-Stages” : Revue de Micropaléontologie, 42, 93–97.Briais, A., Patriat, P., & Tapponnier, P. (1993). Updated interpretation of magnetic anomalies

and seafloor spreading stages in the South China Sea: Implications for the Tertiary tectonics of Southeast Asia. Journal of Geophysical Research: Solid Earth, 98(B4), 6299–6328.

Clift, P.D., Lee, G.H., Nguyen, A.D., Barckhausen, U., Hoang, V.L., Sun, Z. (2008). Seismic evidence for a Dangerous Grounds mini-plate: No extrusion origin for the South China Sea. Tectonics, 27, TC3008.

Cornacchia, I., Brandano, M., Agostini, S. (2021). Miocene paleoceanographic evolution of the Mediterranean area and carbonate production changes: A review. Earth-Science Reviews, 221, 103785.

Davies, P. and Marshall, J. (1985) Halimeda bioherms – low energy reefs, northern Great Barrier Reef. Proceedings of the 5th International Coral Reef Symposium, 1–7.

Ding, W., Li, Jiabiao, L., Dong, C., Fang, Y. (2015). Oligocene–Miocene carbonates in the Reed Bank area, South China Sea, and their tectono-sedimentary evolution. Marine Geophysical Research, 36, 149-165.

Dippner, J. W., Nguyen, K. V., Hein, H., Ohde, T., & Loick, N. (2007). Monsoon-induced upwelling off the Vietnamese coast. Ocean Dynamics, 57(1), 46-62.

Fournier, F., Borgomano, J. (2007). Geological significance of seismic reflections and imaging of the reservoir architecture in the Malampaya gas field (Philippines). AAPG Bulletin, 91, 2, 235–258.

Fournier, F, Montaggioni, L., & Borgomano, J. (2004). Paleoenvironments and high-frequency cyclicity from Cenozoic South-East Asian shallow-water carbonates: A case study from the Oligo-Miocene buildups of Malampaya (Offshore Palawan, Philippines). Marine and Petroleum Geology, 21(1), 1–21.

Fournier, F, Borgomano, J., Montaggioni, L. F. (2005). Development patterns and controlling factors of Tertiary carbonate buildups: Insights from high-resolution 3D seismic and well data in the Malampaya gas field (Offshore Palawan, Philippines). Sedimentary Geology, 175(1-4), 189–215.

Fulthorpe, C.S., Schlanger, S.O. (1989). Paleo-Oceanographic and tectonic settings of early Miocene reefs and associated carbonates of offshore southeast Asia. AAPG Bulletin, 73, 6, 729-756.

Gishler, E., Hudson, J.H. (2004). Holocene development of the Belize Barrier Reef. Sedimentary Geology, 164, 3, 223-236.

Hall, R. (2002). Cenozoic geological and plate tectonic evolution of SE Asia and the SW Pacific: computer-based reconstructions, model and animations. Journal of Asian Earth Sciences, 20, 4, 353–431.

Hallock, P., Schlager, W. (1986). Nutrient excess and the demise of coral reefs and carbonate platforms. Palaios, 1, 389-398.

Hallock, P., Pomar, L. (2009). Cenozoic Evolution of Larger Benthic Foraminifers: Paleoceanographic Evidence for Changing Habitats. Proceedings of the 11 th International Coral Reef Symposium, Ft. Lauderdale, Florida, 7-11 July 2008.

Hallock, P., Hine, A. C., Vargo, G.A., Elrod, J.A, Jaap, W. C. (1988). Platforms of the Nicaraguan Rise: Examples of the sensitivity of carbonate sedimentation to excess trophic resources. Geology, 16, 1104-1107.

Heyward, A., Pinceratto, E. and Smith, L. (1997) Big Bank Shoals of the Timor Sea: an environmental resource atlas. Australian Institute of Marine Science & BHP Petroleum.

Hine, A.C., Hallock, P., Harris, M.W., Mullins, H.T., Belknap, D.F. and Jaap, W.C. (1988). Halimeda bioherms along an open seaway: Miskito Channel, Nicaraguan Rise, SW Caribbean Sea. Coral Reefs, 6, 173–178.

Hutchison, C.S., Bergman, S.C., Swauger, D.A., Graves, J.E. (2000). A Miocene collisional belt in north Borneo: uplift mechanism and isostatic adjustment quantified by thermochronology. Journal of the Geological Society, 157, 783-793.

Khanolkar, S., Saraswati, P.K. (2019). Eocene foraminiferal biofacies in Kutch Basin (India) in context of palaeoclimate and palaeoecology. Journal of Palaeogeography, 8, 21.

Li, C. F., Xu, X., Lin, J., Sun, Z., Zhu, J., Yao, Y., et al. (2014). Ages and magnetic structures

of the South China Sea constrained by deep tow magnetic surveys and IODP Expedition 349. Geochemistry, Geophysics, Geosystems, 15, 4958–4983.

Licht, A., van Cappelle, M., Abels, H.A., Ladant, J.B., Trabucho-Alexandre, J., France-Lanord, C., Donnadieu, Y., Vandenberghe, J., Rigaudier, T., Lecuyer, C., Terry Jr, D., Adriaens, R., Boura, A., Guo, Z., Soe, A.N., Quade, J., Dupont-Nivet, G., Jaeger, J.J. (2014). Asian monsoons in a late Eocene greenhouse world. Nature, 513, 501–506.

Licht, A., Dupont-Nivet, G., Pullen, A., Kapp, P., Abels, H. A., Lai, Z., Guo, Z., Abell, J., Giesler, D. (2016). Resilience of the Asian atmospheric circulation shown by Paleogene dust provenance. Nature communications, 7(1), 1-6.

Lunt, P., and Renema, W., 2014. On the Heterostegina– Tansinhokella– Spiroclypeus lineage(s) in SE Asia. Berita Sedimentologi, 30, 6-31.

Mathew, M., Makhankova, A., Menier, D., Sautter, B., Betzler, C., Pierson, B., (2020). The emergence of Miocene reefs in South China Sea and its resilient adaptability under varying eustatic, climatic and oceanographic conditions. Scientific Reports, 10, 7141.

McNeil, M.A., Nothdurft, L.D., Dyriw, N.J., Webster, J.M., Beaman, R.J. (2020). Morphotype differentiation in the Great Barrier Reef Halimeda bioherm carbonate factory: internal architecture and surface geomorphometrics. The Depositional Record 7, 176-199.

Meijer, N., Dupont-Nivet, G., Barbolini, N., Woutersen, A., Rohrmann, A., Zhang, Y, Liu, X.-J., Licht, A., Abels, H.A., Hoorn, C., Tjallingii, R., Andermann, C., Dietze, M., Nowaczyk, N. (2021). Loess-like dust appearance at 40 Ma in central China. Paleoceanography and Paleoclimatology, 36(3), e2020PA003993.

Morley, C.K. (2012). Late Cretaceous–Early Palaeogene tectonic development of SE Asia. Earth-Science Reviews, 115, 37–75.

585 Morley C. K. (2016). Major unconformities/termination of extension events and associated
586 surfaces in the South China Seas: review and implications for tectonic development. Journal of
587 Asian Earth Sciences, 120, 62–86.

588 Mutti, M., Hallock, P., 2003. Carbonate systems along nutrient and temperature gradients: some
589 sedimentological and geochemical constraints. Int. J. Earth Sci. 92, 465–475.

590 Page, M., Licht, A., Dupont-Nivet, G., Meijer, N., Barbolini, N., Hoorn, C., Schauer, A.,
591 Huntington, K., Bajnai, D., Fiebig, A., Mulch, A., Guo, Z. (2019). Synchronous cooling and
592 decline in monsoonal rainfall in northeastern Tibet during the fall into the Oligocene icehouse.
593 Geology, 47(3), 203-206.

594 Pomar, L. (2001). Ecological control of sedimentary accommodation: Evolution from a
595 carbonate ramp to rimmed shelf, Upper Miocene, Balearic Islands. Palaeogeography
596 Palaeoclimatology Palaeoecology, 175(1–4), 249–272.

597 Pomar, L., Morsilli, M., Hallock, P., and Bádenas, B. (2012). Internal waves, an under-explored
598 source of turbulence events in the sedimentary record. Earth-Science Reviews, 111, 1–2, 56–
599 81.

600 Pomar, L., Mateu-Vicens, G., Morsilli, M., and Brandano, M. (2014). Carbonate ramp evolution
601 during the Late Oligocene (Chattian), Salento Peninsula, southern Italy: Palaeogeography
602 Palaeoclimatology Palaeoecology, 404, 109-132.

603 Quan, C., Liu, Y.-S., Utescher, T. (2012). Eocene monsoon prevalence over China: A
604 paleobotanical perspective. Palaeogeography, Palaeoclimatology, Palaeoecology 365–366,
605 302–311.

606 Reijmer, J.J.G., Betzler, C., Kroon, D., Tiedemann, R., Eberli, G.P. (2002). Bahamian
607 carbonate platform development in response to sea-level changes and the closure of the Isthmus
608 of Panama. International Journal of Earth Sciences, 91, 482–489.

609 Renema, W., 2007. Chapter 6: Fauna Development of Larger Benthic Foraminifera in the
610 Cenozoic of Southeast Asia. In: W. Renema (ed.), Biogeography, Time and Place:
611 Distributions, Barriers and Islands, 179—215.

612 Roberts, H.H., Aharon, P. and Phipps, C.V. (1988) Morphology and sedimentology of
613 Halimeda bioherms from the eastern Java Sea (Indonesia). Coral Reefs, 6, 161–172.

614 Roberts, H.H., Wilson, P.A., Lugo-Fernandez, A. (1992). Biologic and geologic responses to
615 physical processes: examples from modern reef systems of the Caribbean-Atlantic region.
616 Continental Shelf Research, 12, 809-834.

617 Romero, J., Caus, E., Rosell, J. (2002). A model for the palaeoenvironmental distribution of
618 larger foraminifera based on late Middle Eocene deposits on the margin of the South Pyrenean
619 basin (NE Spain). Palaeogeography, Palaeoclimatology, Palaeoecology, 179, 1-2, 43-56.

620 Sarr, A.T., Donnadieu, Y., Bolton, C.T., Ladant, J.B., Licht, A., Fluteau, F., Laugié, M., Tardif,
621 D., Dupont-Nivet, G. (2022). Neogene South Asian monsoon rainfall and wind histories
622 diverged due to topographic effects. Nature Geoscience, 15, 314–319.

623 Searle, D. and Flood, P. (1988). Halimeda bioherms of the Swain reefs– southern Great Barrier
624 Reef. Proceedings of the 6th International Coral Reef Symposium, 139–144.

625 Shao, L., Cao, L., Qiao, P., Zhang, P., Li, Q., van Hinsbergen, D.J.J. (2017). Cretaceous–Eocene
626 provenance connections between the Palawan Continental Terrane and the northern South
627 China Sea margin. Earth and Planetary Science Letters, 477, 97–107.

628 Sinclair, H.D., Sayer, Z.R., Tucker, M.E. (1998). Carbonate sedimentation during early
629 foreland basin subsidence: the Eocene succession of the French Alps. In: Wright,V. R &
630 Burchette,T. R (eds) Carbonate Ramps. Geological Society, London, Special Publications, 149,
631 205-227.

632 Sorrel, P., Eymard, I., Leloup, P.-H., Maheo, G., Olivier, N., Sterb, M., Gourbet, L., Wang, G.,
633 Jing, W., Lu, H., Li, H., Yadong, X., Zhang, K., Cao, K., Chevalier, M.-L., Replumaz, A., 2017.
634 Wet tropical climate in SE Tibet during the Late Eocene. Scientific Reports, 7, 7809.

635 Spicer, R. A., Yang, J., Herman, A. B., Kodrul, T., Maslova, N., Spicer, T.E.V, Aleksandrova,
636 G., Jin, J. (2016). Asian Eocene monsoons as revealed by leaf architectural signatures. Earth
637 and Planetary Science Letters, 449, 61-68.

638 Steuer, S., Franke, D., Meresse, F., Savva, D., Pubellier, M., Auxietre, J. L. (2014). Oligocene-
639 Miocene carbonates and their role for constraining the rifting and collision history of the
640 Dangerous Grounds, South China Sea. Marine and Petroleum Geology, 58(PB), 644–657.

641 Sun, R., Li, Z., Zhao, Z., Yang, H., Wang, X., Zhao, Z. (2020). Characteristics and origin of the
642 Lower Oligocene marine source rocks controlled by terrigenous organic matter supply in the
643 Baiyun Sag, northern South China Sea. Journal of Petroleum Science and Engineering, 187,
644 106821.

645 Tardif, D., Fluteau, F., Donnadieu, Y., Le Hir, G., Ladant, J.-B., Sepulchre, P., Licht, A.,
646 Poblete, F., and Dupont-Nivet, G. (2020). The origin of Asian monsoons: a modelling
647 perspective, Climate of the Past, 16, 847–865.

648 Toumoulin, A., Tardif, D., Donnadieu, Y., Licht, A., Ladant, J. B., Kunzmann, L., & Dupont-
649 Nivet, G. (2022). Evolution of continental temperature seasonality from the Eocene greenhouse
650 to the Oligocene icehouse–a model–data comparison. Climate of the Past, 18(2), 341-362.

651 Utama, F.G., Atmadipoera, A.S., Purba, M., Sudjono, E.H., Zuraida, R. (2017). Analysis of
652 upwelling event in Southern Makassar Strait. IOP Conf. Series: Earth and Environmental
653 Science, 54, 012085.

654 Wheeler, M. C., & McBride, J. L. (2005). Australian-indonesian monsoon. In Intraseasonal
655 variability in the atmosphere-ocean climate system (pp. 125-173). Springer, Berlin, Heidelberg.

656 Wu, F., Xie, X., Li, X., Betzler, C., Shang, Z., Cui, Y. (2019). Carbonate factory turnovers
657 influenced by the monsoon (Xisha Islands, South China Sea). Journal of the Geological Society,
658 176, 885-897.

659 Zahirovic, S., Seton, M., Müller, R.D. (2014). The Cretaceous and Cenozoic tectonic evolution
660 of Southeast Asia. Solid Earth, 5, 227–273.

661 Zheng, H., Yang, Q., Cao, S., Clift, P.D., He, M., Kano, A., Sakuma, A., Xu, H., Tada, R.,
662 Jourdan, F. (2022). From desert to monsoon: irreversible climatic transition at ~ 36 Ma in
663 southeastern Tibetan Plateau. Progress in Earth and Planetary Science, 9(1): 12.

664 Zhou, D., Ru, K., Chen, H.-Z. (1995). Kinematics of Cenozoic extension on the South China
665 Sea continental margin and its implications for the tectonic evolution of the region.
666 Tectonophysics, 251, 1, 161-177.

Figure and Table caption

Figure 1: (A) East Asia today with modern summer EAM winds (red arrows); SCJ: Summer Coastal Jet; SCS: South China Sea; (B) East Asia in the late Eocene (after Poblete et al., 2020); red line: SCS rift; black line: North Borneo subduction zone. CPBC: Calamian–North Palawan–North Borneo micro-continent. Our study site is indicated by a yellow star on both figures, blue colors indicate marine areas (dark blue: abyssal depths; light blue: continental shelf); green to brown colors indicate emerged areas (green: low altitude; brown: high altitude).

Figure 2: A) Location map of the Malamapaya carbonate platform, B) Regional seismic profile showing the development of the Malampaya buildup on the crest of a tilted block. C) Depth map in meters of the top Nido surface and well location (from Fournier et al., 2004). D) Lithostratigraphic column of the Malampaya platform, name and age of the main sedimentary units (modified after Fournier and Borgomano, 2007).

Figure 3: Correlation panel between wells Malampaya-1, -2 and -5 and correspondence between depositional units and seismic markers. (after Fournier and Borgomano, 2007). Well location is reported on **Fig. 2C, Fig. 6** and **Fig. 7**.

Figure 4: **A:** Malampaya-2 well: porosity and sonic logs, sequences (after Fournier and Borgomano, 2007), seismic markers, distribution of foraminiferal taxa and biostratigraphic interpretations; **B:** Letter-Stage classification (after Boudagher-Fadel and Banner, 1999; Renema, 2007) and the key benthonic foraminiferal taxa used in the present work.

Figure 5: Porosity and sonic logs, sequences (after Fournier and Borgomano, 2007), seismic markers, distribution of foraminiferal taxa and biostratigraphic interpretations following the Letter-Stage classification. **A:** Malampaya-1 well; **B:** Malampaya-5 well.

Figure 6: Uninterpreted (**A**) and interpreted (**B**) seismic profile (crossline XL1935); **C**) Two-way-time surface of Top Late Eocene (R10.1 reflector) and Top Early Rupelian buildups (R10.2 reflector) and location of crossline XL1935 (**A-B**).

Figure 7: Uninterpreted (**A**) and interpreted (**B**) arbitrary line crossing buildups A, B,C, D and well Malampaya-2 (location on **C** and **D**); **C**) Two-way-time (TWT) thickness of early Rupelian unit SR1; **D**) Isochron map of Top Early Rupelian (R10.2 reflector).

Figure 8: Average grain composition of Upper Eocene (FE1, FE2), Lower Rupelian (FR1, FR2 and FR3) and Upper Rupelian (FR4) facies.

Figure 9: Thin section microphotograph of Late Eocene microfacies: A-B) Quartz-rich, foraminiferal-coralline algal grainstone (Facies FE1); C-D) Quartz-bearing, bryozoan, foraminiferal, coralline algal packstone. Disc.: Discocyclina; Bry.: bryozoan; CA: coralline algae; Qz: quartz grains (Qz).

Figure 10: A-B-C-D) Thin section microphotograph of early Rupelian microfacies (Facies FR1): *Halimeda*-rudstone showing random or vertically-oriented Halimeda segments (Hal.), scarce coral branches (Cor.), flat-shaped large benthic foraminifers (LBF), geopetal peloidal matrix infills (pm) and homogeneous micrite infill postdating isopacheous bladed calcite cements (black arrow); **E-F**) Thin section microphotograph of early Rupelian microfacies FR2: Coralline algal-foraminiferal-*Halimeda* packstone (FR2) with sparse pteropod (white arrow), *Nummulites* (Num.) and solitary coral (SC); G) Core photograph of macrofacies FR3: Rhodolithic floatstone (Rho.: rhodolith).

Figure 11: Malampaya-2 well : well-logs, vertical facies distribution, grain composition (point-counting) and facies associations.

713 **Figure 12:** Growth pattern of the carbonate buildups of Malampaya from the late Eocene to
714 the early Miocene in relation to tectonic evolution and paleoceanographic changes.

715

716 **Table 1**: Morphologic features of buildups A, B, C and D.

717

718

Supplementary material

Supplementary Material S1: MA-2 well: well-to seismic tie and interval velocities.

Supplementary Material S2: Grain composition from point-counting on thin-sections.

Supplementary Material S3: Summary of published modern *Halimeda* bioherms and their geomorphologic and sedimentologic features.

Figure 01

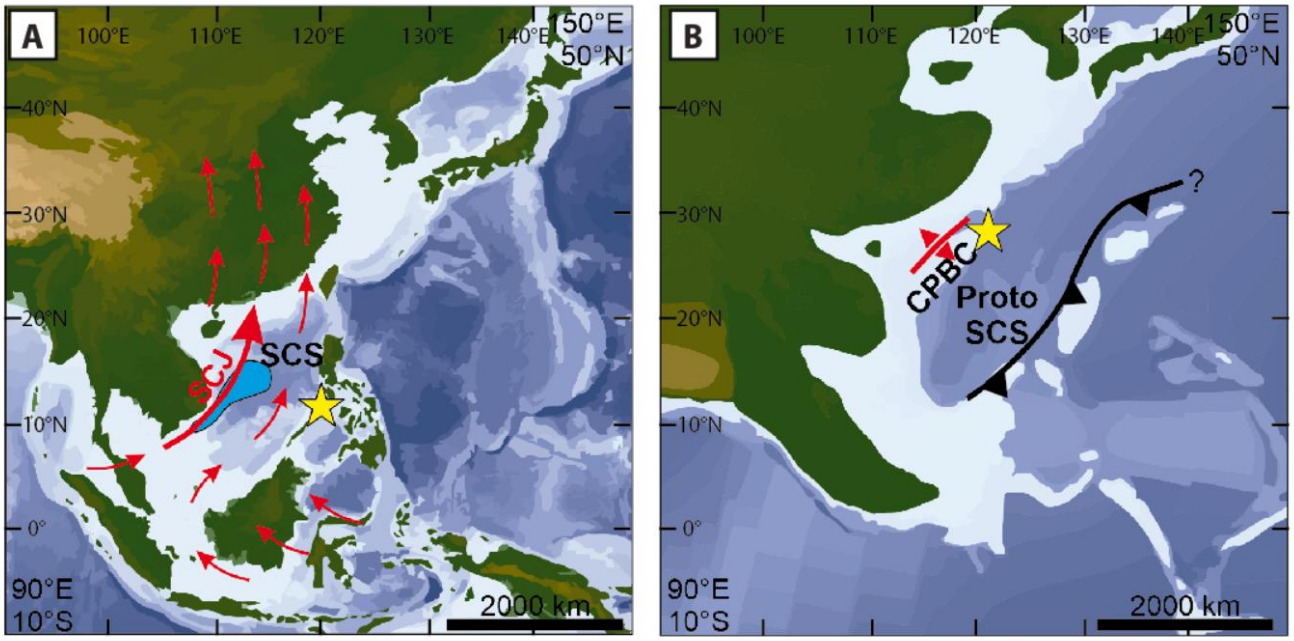

Figure 1: (A) East Asia today with modern summer EAM winds (red arrows); SCJ: Summer Coastal Jet; SCS: South China Sea; (B) East Asia in the late Eocene (after Poblete et al., 2020); red line: SCS rift; black line: North Borneo subduction zone. CPBC: Calamian–North Palawan–North Borneo micro-continent. Our study site is indicated by a yellow star on both figures, blue colors indicate marine areas (dark blue: abyssal depths; light blue: continental shelf); green to brown colors indicate emerged areas (green: low altitude; brown: high altitude).

Figure 02

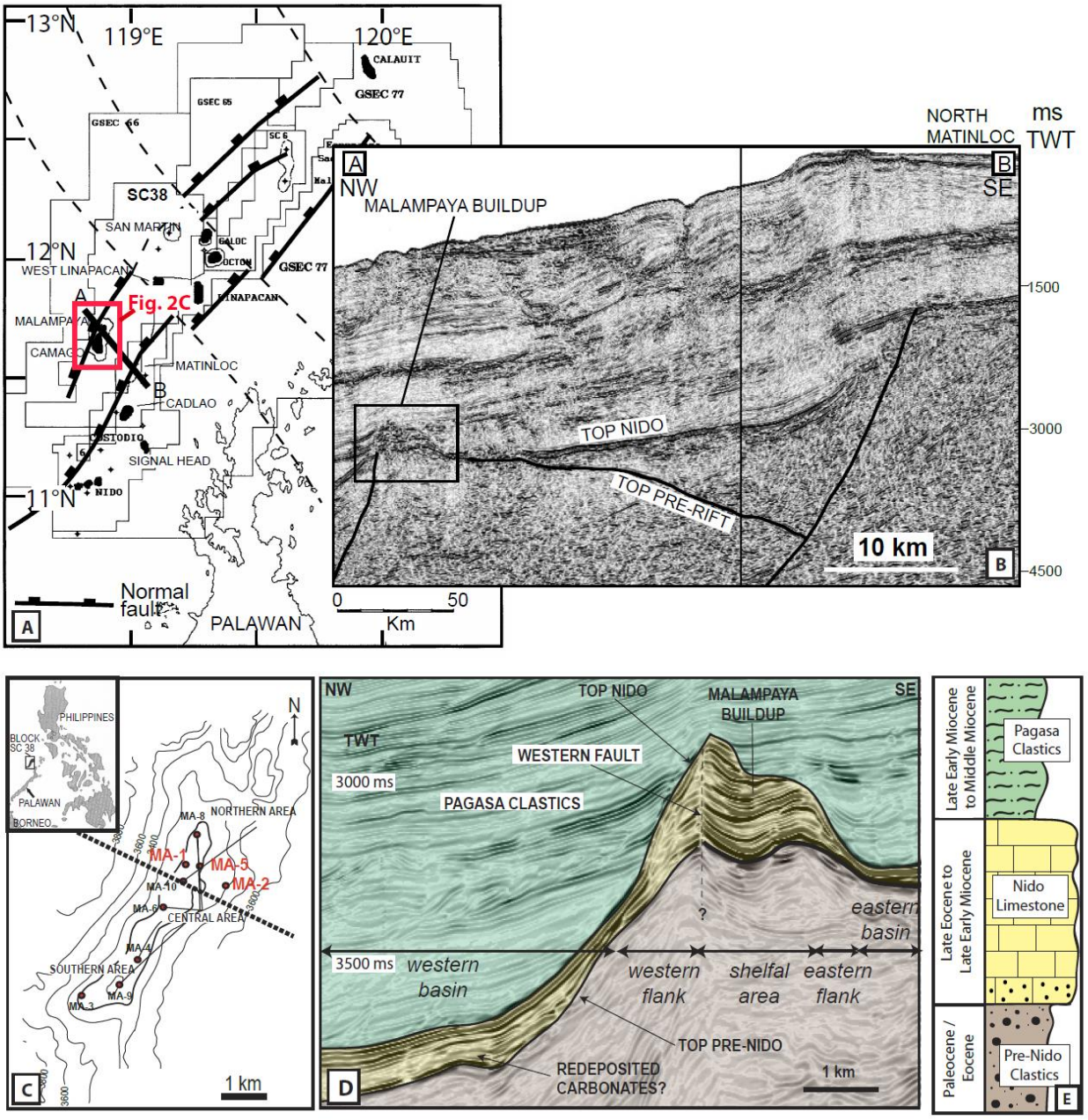

Figure 2: A) Location map of the Malamapaya carbonate platform, B) Regional seismic profile showing the development of the Malampaya buildup on the crest of a tilted block. C) Depth map in meters of the top Nido surface and well location (from Fournier et al., 2004). D) Lithostratigraphic column of the Malampaya platform, name and age of the main sedimentary units (modified after Fournier and Borgomano, 2007).

Figure 03

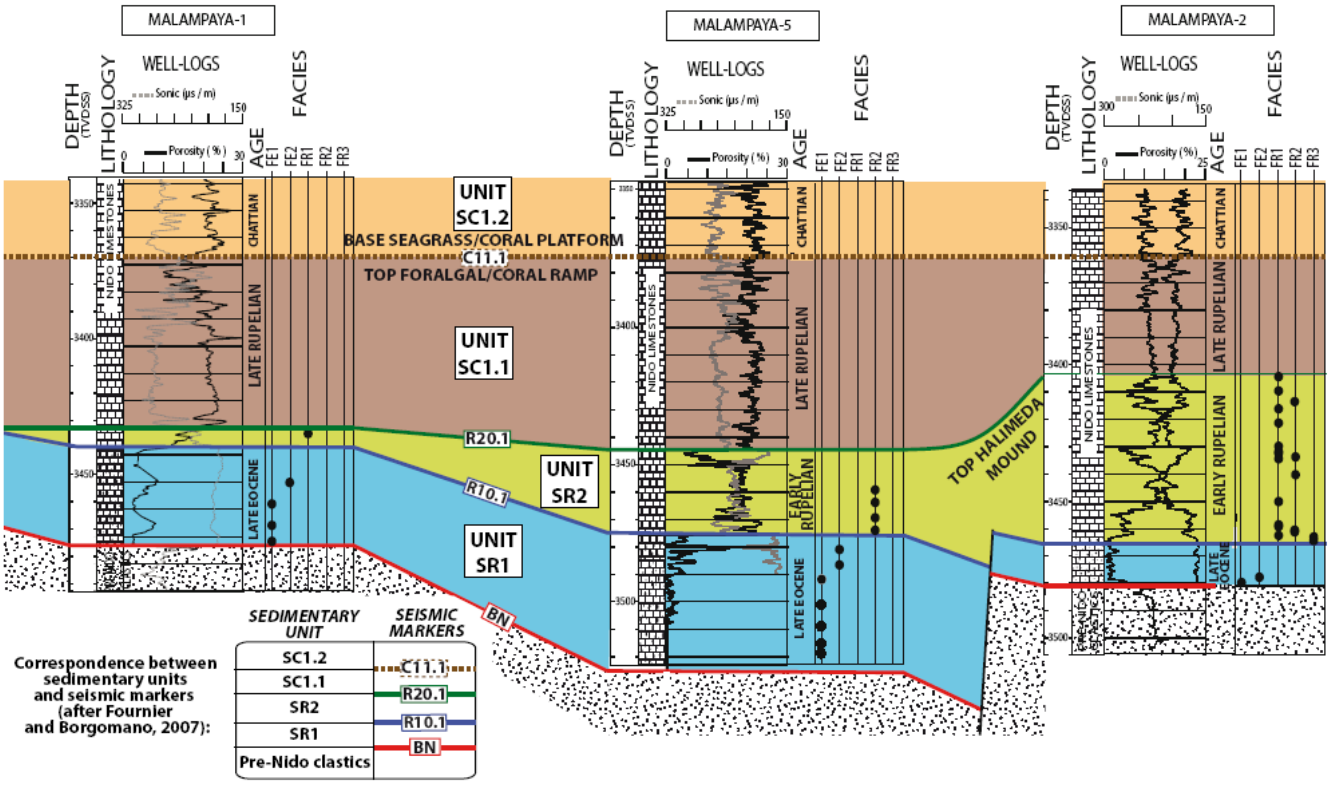

Figure 3: Correlation panel between wells Malampaya-1, -2 and -5 and correspondence between depositional units and seismic markers. (after Fournier and Borgomano, 2007).

Figure 04

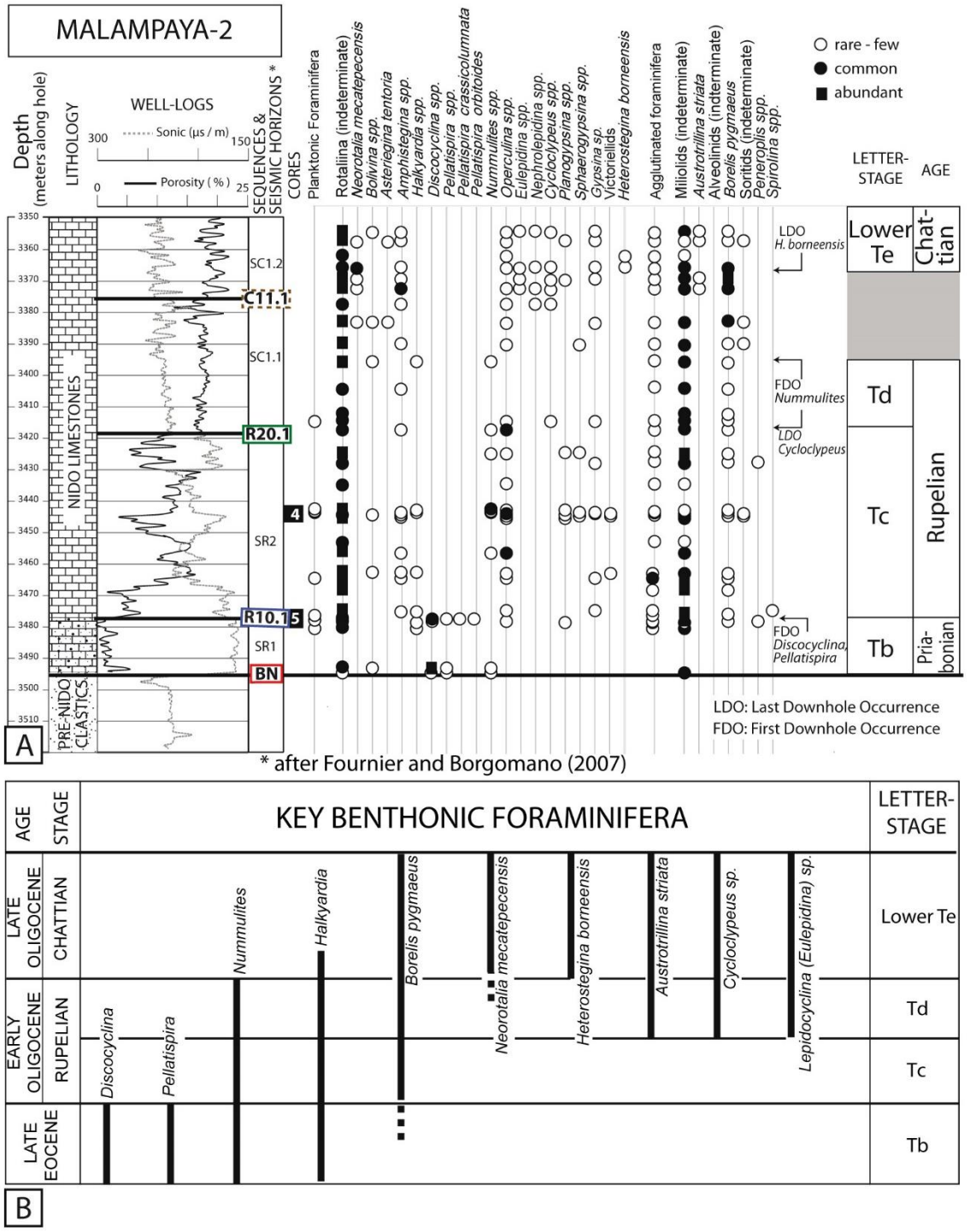

Figure 4: **A:** Malampaya-2 well: porosity and sonic logs, sequences (after Fournier and Borgomano, 2007), seismic markers, distribution of foraminiferal taxa and biostratigraphic interpretations; **B:** Letter-Stage classification (after BouDadher-Fadel and Banner, 1999; Renema, 2007) and the key benthonic foraminiferal taxa used in the present work.

Figure 05

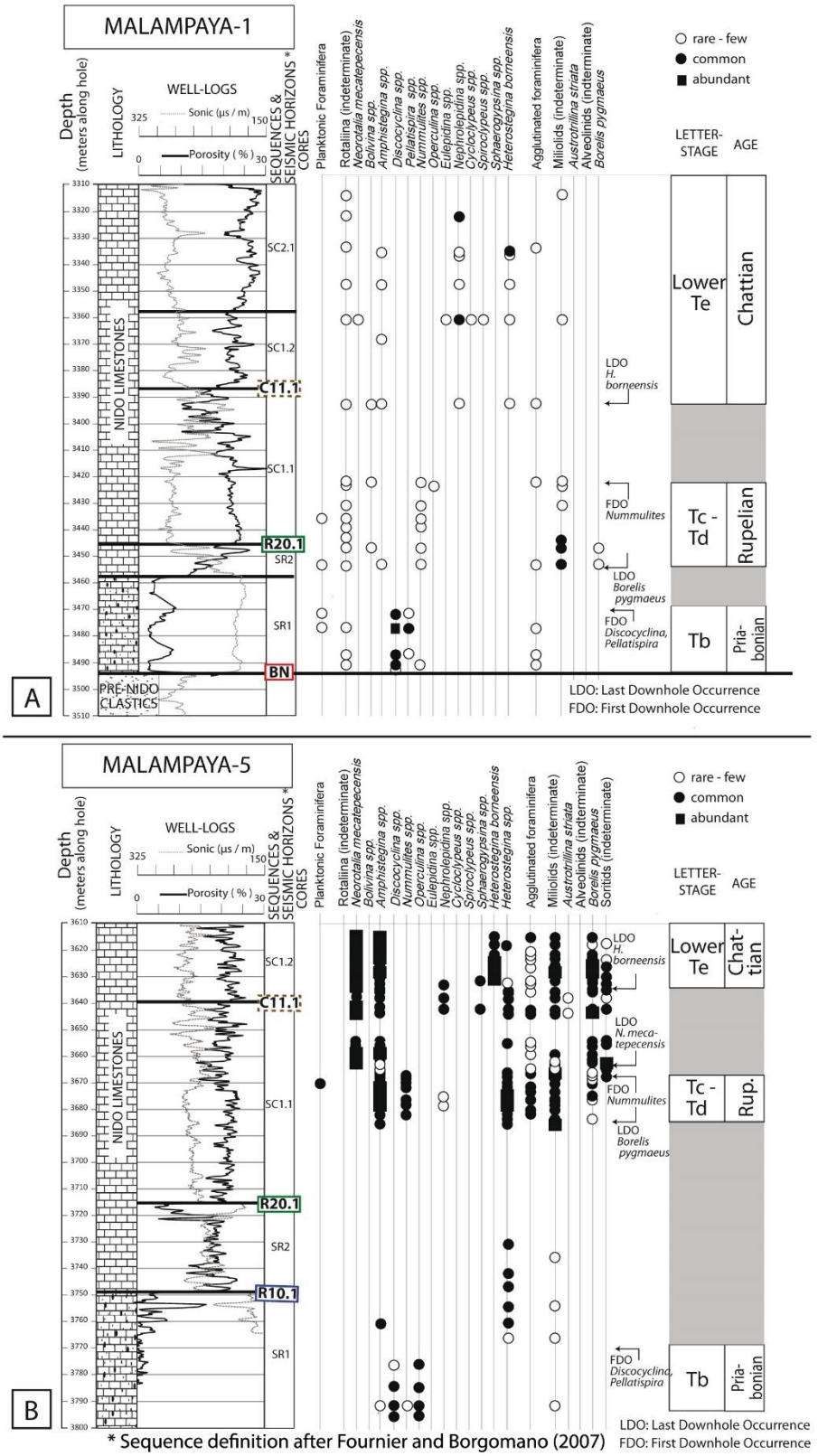

Figure 5: Porosity and sonic logs, sequences (after Fournier and Borgomano, 2007), seismic markers, distribution of foraminiferal taxa and biostratigraphic interpretations following the Letter-Stage classification. **A:** Malampaya-1 well; **B:** Malampaya-5 well.

Figure 06

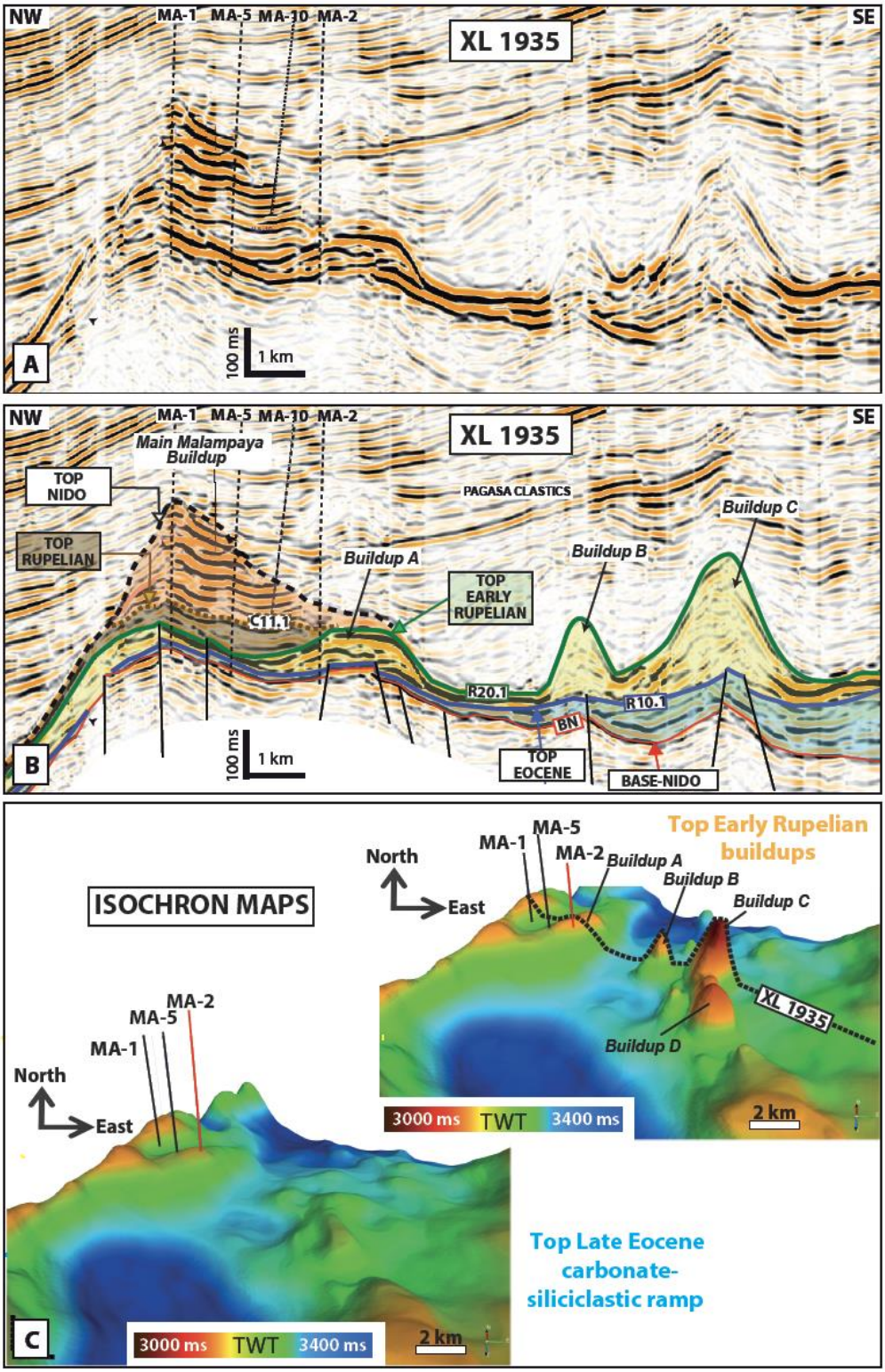

Figure 6: Uninterpreted (**A**) and interpreted (**B**) seismic profile (crossline XL1935); **C**) Two-way-time surface of Top Late Eocene (R10.1 reflector) and Top Early Rupelian buildups (R10.2 reflector) and location of crossline XL1935 (**A-B**).

Figure 07

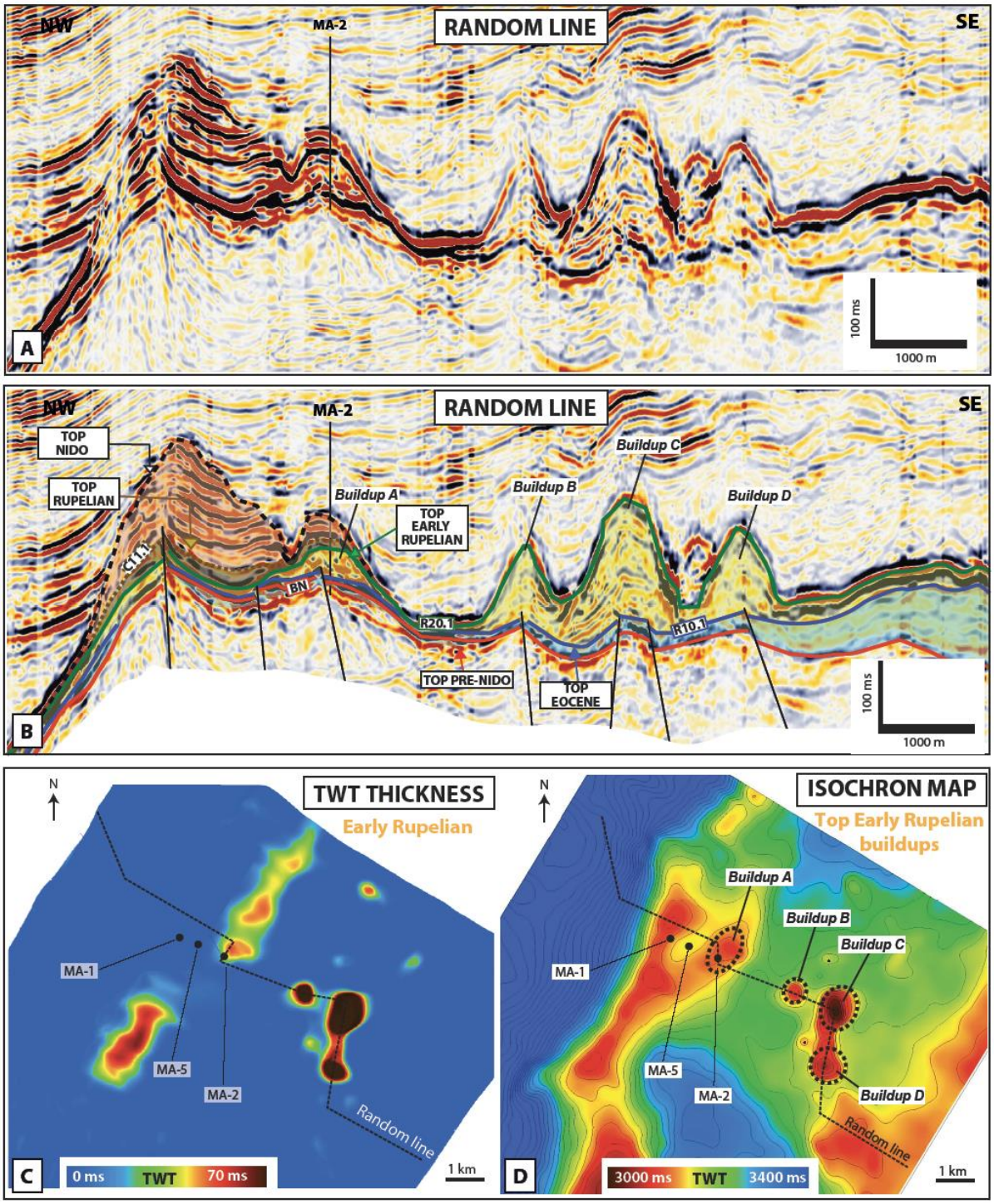

Figure 7: Uninterpreted (**A**) and interpreted (**B**) arbitrary line crossing buildups A, B,C, D and well Malampaya-2 (location on **C** and **D**); **C**) Two-way-time (TWT) thickness of early Rupelian unit SR1; **D**) Isochron map of Top Early Rupelian (R10.2 reflector).

Figure 08

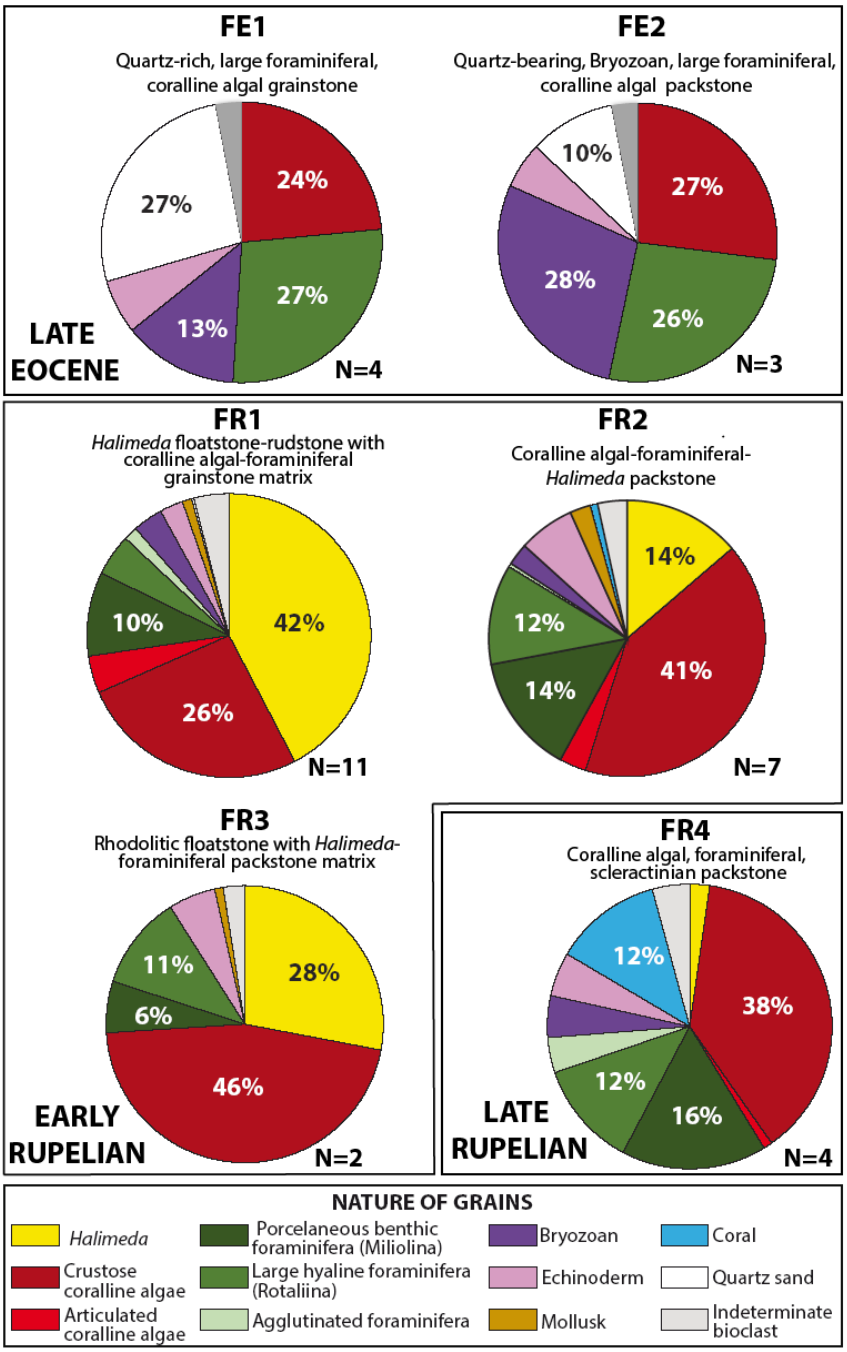

Figure 8: Average grain composition of Upper Eocene (FE1, FE2), Lower Rupelian (FR1, FR2 and FR3) and Upper Rupelian (FR4) facies.

Figure 09

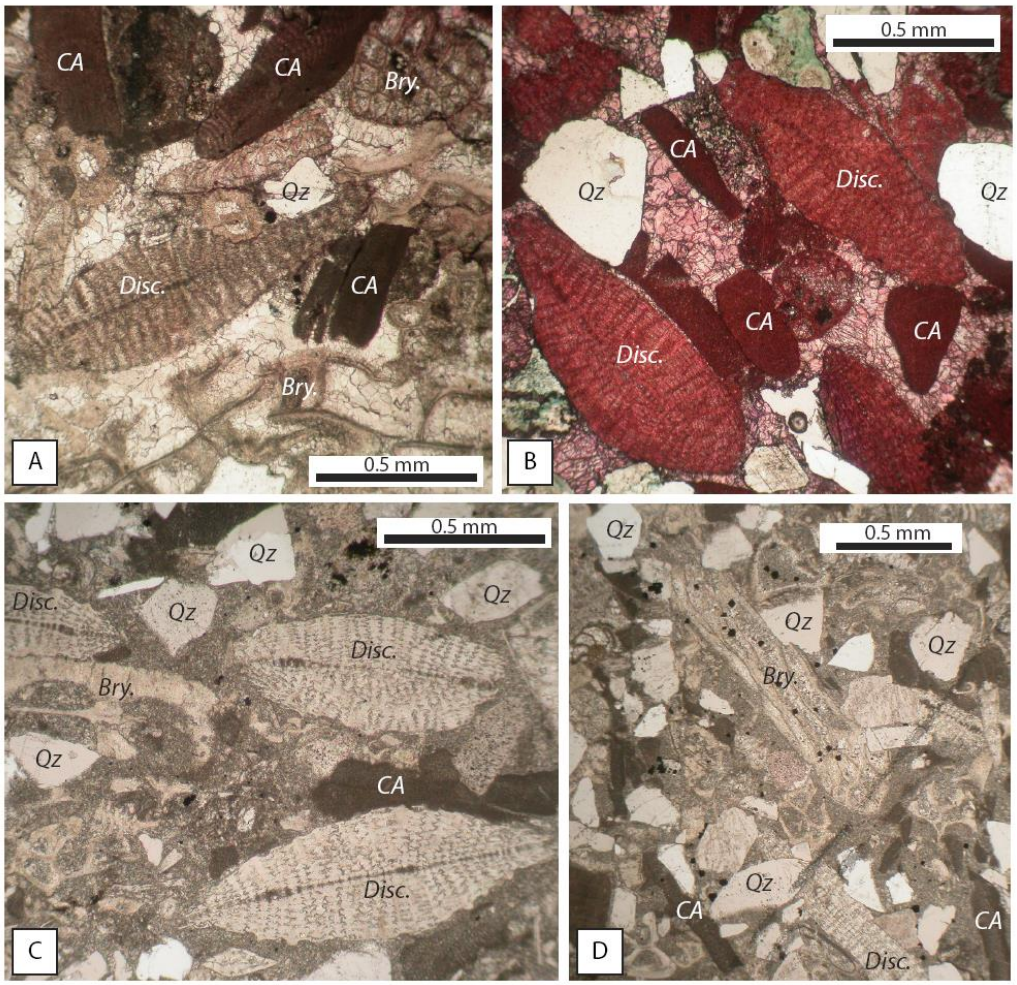

Figure 9: Thin section microphotograph of Late Eocene microfacies: A-B) Quartz-rich, foraminiferal-coralline algal grainstone (Facies FE1); C-D) Quartz-bearing, bryozoan, foraminiferal, coralline algal packstone. Disc.: Discocyclina; Bry.: bryozoan; CA: coralline algae; Qz: quartz grains (Qz).

Figure 10

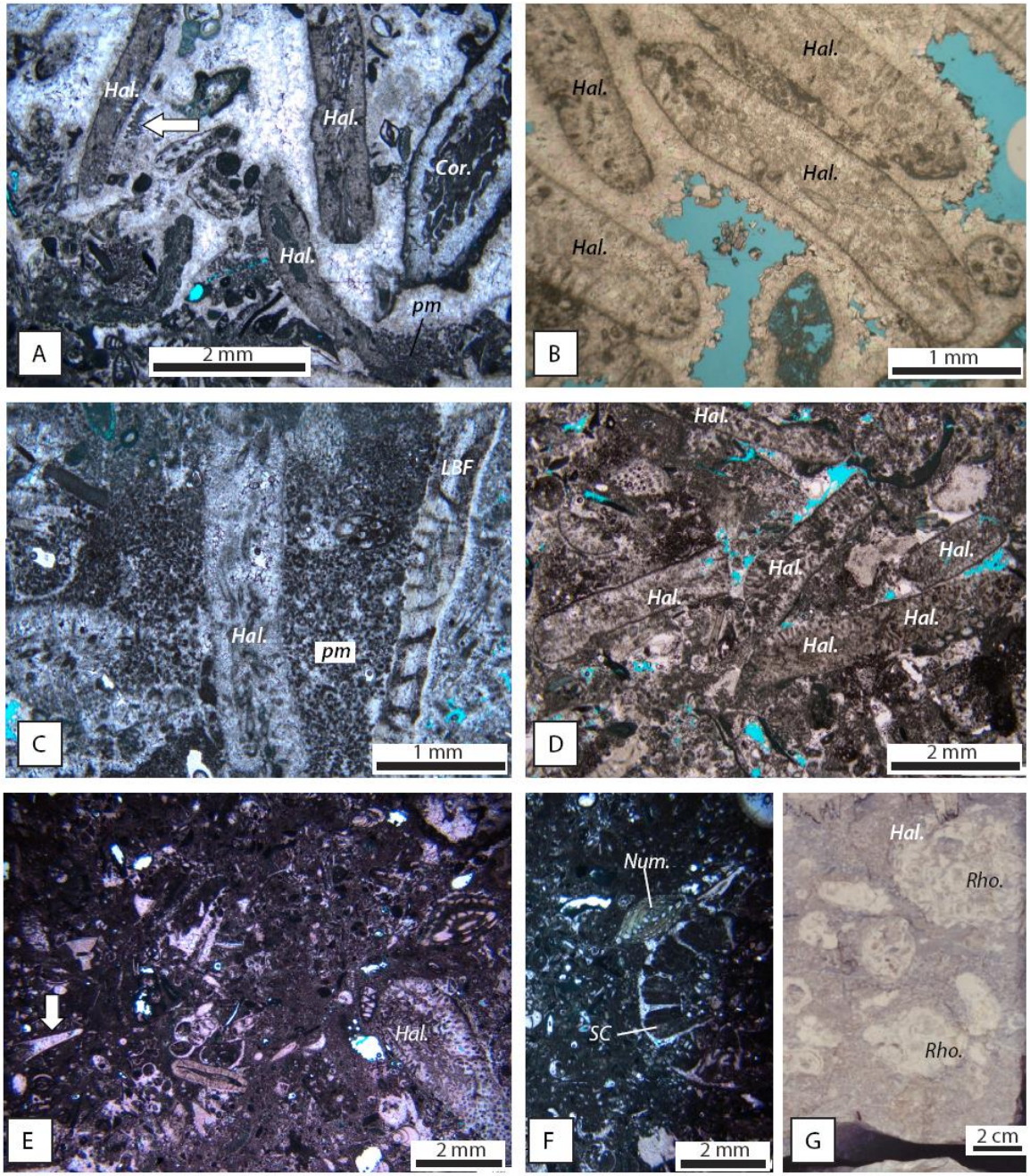

Figure 10: **A-B-C-D**) Thin section microphotograph of early Rupelian microfacies (Facies FR1): *Halimeda*-rudstone showing random or vertically-oriented Halimeda segments (Hal.), scarce coral branches (Cor.), flat-shaped large benthic foraminifers (LBF), geopetal peloidal matrix infills (pm) and homogeneous micrite infill postdating isopacheous bladed calcite cements (black arrow); **E-F**) Thin section microphotograph of early Rupelian microfacies FR2: Coralline algal-foraminiferal-*Halimeda* packstone (FR2) with sparse pteropod (white arrow), *Nummulites* (Num.) and solitary coral (SC); G) Core photograph of macrofacies FR3: Rhodolithic floatstone (Rho.: rhodolith).

Figure 11

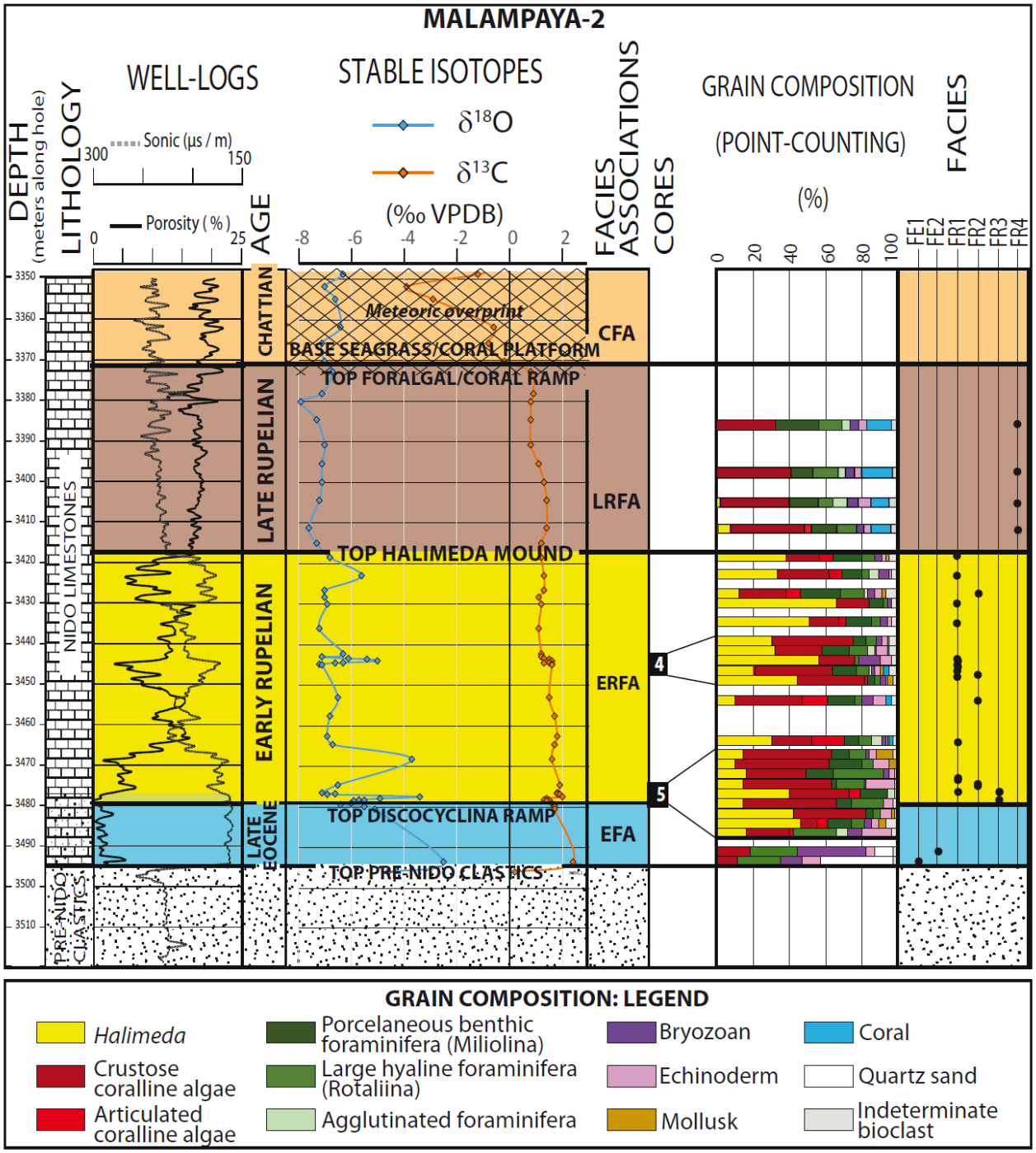

Figure 11: Malampaya-2 well : well-logs, vertical facies distribution, grain composition (point-counting) and facies associations.

Figure 12

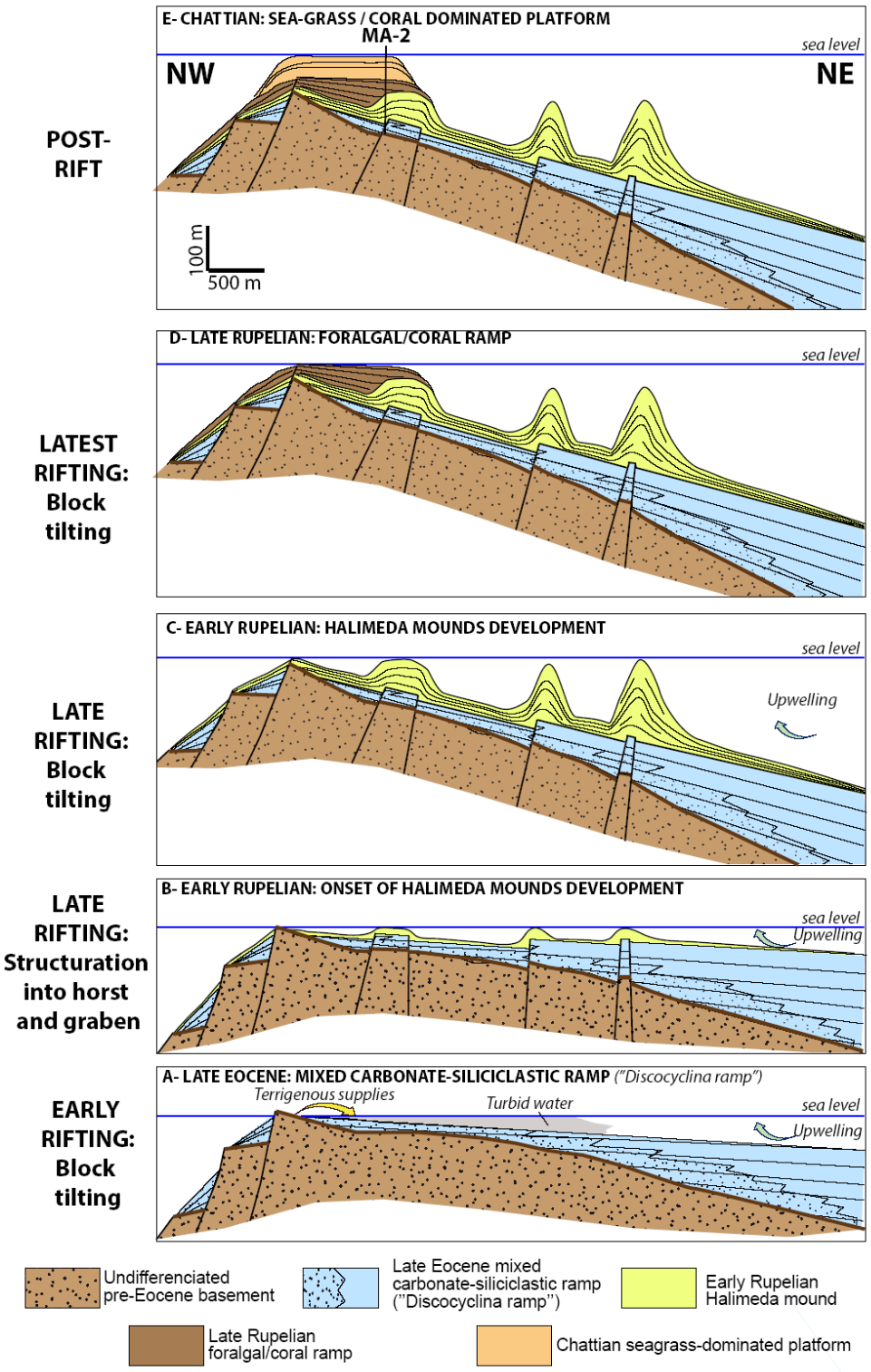

Figure 12: Growth pattern of the carbonate buildups of Malampaya from the late Eocene to the early Miocene in relation to tectonic evolution and paleoceanographic changes.

Table 1

	Maximum TWT thickness (ms)	Estimated maximum thickness (m)	Buildup diameter at base (m)	Dip angle of buildup flanks (top buildup surface)
Buildup A	50	125	1100	21°
Buildup B	150	380	850	42°
Buildup C	220	580	1300	40°
Buildup D	130	330	800	39°

Table 1 : Morphologic features of buildups A, B, C and D.

Supplementary Material S1

Sedimentary unit	Surface	Seismic Marker	Seismic TWT (ms)	Depth at well (meters, TVDSS)	Interval Velocity (m/s)	
					From well-to-seismic tie	From integration of sonic log
	Top early Rupelian	R20.1	3125	3402		
Early Rupelian (SR2)	-	-	-	-	5040	5070
	Top Eocene	R10.1	3150	3465		
Late Eocene (SR1)					-	6333
	Base Nido	BN	3170	3480		
Pre-Nido clastics					-	4234

Supplementary Material S1: **:** MA-2 well: well-to seismic tie and interval velocities.

Supplementary Material S2

Well	depth (meters along hole)		Halimeda	Encrusting RA	Articulated RA	Porcelaneous F.	Rotaliina	Textulariina	Bryozoan	Echinoderm	mollusks	coral	Qz	indet.
MA-1	3492	FE1	0	27	0	0	35	0	10	5	0	0	20	3
MA-1	3491	FE1	0	32	0	0	28	0	15	4	0	0	18	3
MA-1	3486	FE1	0	24	0	0	23	0	16	6	0	0	28	3
MA-1	3477	FE2	0	28	0	0	29	0	27	5	0	0	8	3
MA-1	3470	FE2	0	35	0	0	24	0	20	6	0	0	12	3
MA-2	3478,45	FR3	42	40	0	4	4	0	0	6	2	0	0	2
MA-2	3477,88	FR3	14	52	0	8	18	0	0	5	0	0	0	3
MA-2	3477,46	FR1	40	33	6	15	0	4	0	0	0	0	0	2
MA-2	3476,85	FR2	14	49	0	3	15	0	1	16	0	0	0	2
MA-2	3476,7	FR2	16	33	0	15	28	0	3	3	0	0	0	2
MA-2	3476,47	FR2	10	52	0	18	6	0	0	9	4	0	0	1
MA-2	3475	FR2	14	49	0	10	9	0	2	4	9	0	0	3
MA-2	3463	FR1	30	22	18	8	7	6	2	1	1	2	0	3
MA-2	3453	FR2	10	37	14	15	4	0	6	7	0	3	0	4
MA-2	3447,3	FR1	44	37	2	4	3	0	3	1	3	0	0	3
MA-2	3445	FR2	20	42	0	15	7	1	2	3	2	3	0	5
MA-2	3444,62	FR1	56	20	0	0	2	0	12	6	0	0	0	4
MA-2	3443,9	FR1	32	26	0	15	10	4	1	6	0	1	0	5
MA-2	3442	FR1	30	45	0	7	6	0	3	3	1	0	0	5
MA-2	3436,5	FR1	51	16	4	14	5	0	4	2	0	0	0	4
MA-2	3430	FR1	66	18	0	8	2	0	2	0	0	0	0	4
MA-2	3428,5	FR2	12	26	8	22	13	2	4	4	2	0	0	7
MA-2	3423,5	FR1	33	29	7	11	4	5	6	1	0	0	0	4
MA-2	3415,5	FR1	38	18	8	16	7	0	4	2	2	0	0	5
MA-2	3411,5	FR4	7	41	4	14	11	0	4	4	0	11	0	4
MA-2	3405	FR4	2	38	0	16	8	8	6	7	0	10	0	5
MA-2	3397	FR4	0	41	0	12	14	4	5	4	0	17	0	3
MA-2	3385	FR4	0	32	0	24	15	4	4	5	0	11	0	5

Supplementary Material S2: Grain composition from point-counting on thin-sections.

Supplementary Material S3

Modern Halimeda bioherms	*Reference*	*water-depth (at top)*	*Thickness*	*diameter at base*	*slope angle*	*Biota*	*Texture*
Miskito Channel, Nicaraguan Rise, SW Caribbean Sea	Hine et al., 1988	40-50m	up to 140 m	up to 750 m	10-25°	Unbroken Halimeda segment, mollusks, echinoderms, rhodoliths	Packstone-grainstone
Kalukalukuang Bank, eastern Java Sea (Indonesia)	Roberts et al, 1987; Phipps and Roberts, 1988	20-40m	20-50m	~100-200m	10-30°	Disarticulated Halimeda plates, foraminifers	Rudstone-floatstone
Big Bank Shoals, Timor Sea, Australia	Heyward et al., 1997	28-45m					
Northern Great Barrier Reef, Australia	Orme et al., 1978; Davies and Marshall, 1985; Drew and Abel, 1988; Marshall and Davies, 1988; Mc Neil et al., 2016, 2020, 2022)	20-40m	5-20m		10-15°	Halimeda segments (>60%), benthic foraminifers (soritids, alveolinids)	Unconsolidated packstone to floatstone-rudstone
Southern Great Barrier Reef, Australia	Searle and Flood (1988)	20-30m	up to 14m				

Supplementary Material S3: **:** Summary of published modern *Halimeda* bioherms and their geomorphologic and sedimentologic features.

REFERENCES OF APPENDIX A6

Davies, P. and Marshall, J. (1985) Halimeda bioherms – low energy reefs, northern Great Barrier Reef. Proceedings of the 5th International Coral Reef Symposium, 1–7.

Drew, E. and Abel, K. (1985). Biology, sedimentology and geography of the vast inter-reefal Halimeda meadows within the Great Barrier Reef Province. Proceedings of the 5th International Coral Reef Symposium, 15–20.

Heyward, A., Pinceratto, E. and Smith, L. (1997) Big Bank Shoals of the Timor Sea: an environmental resource atlas. Australian Institute of Marine Science & BHP Petroleum.

Hine, A.C., Hallock, P., Harris, M.W., Mullins, H.T., Belknap, D.F. and Jaap, W.C. (1988). Halimeda bioherms along an open seaway: Miskito Channel, Nicaraguan Rise, SW Caribbean Sea. Coral Reefs, 6, 173–178.

Marshall, J.F. and Davies, P.J. (1988) Halimeda bioherms of the northern Great Barrier Reef. Coral Reefs, 6, 139–148.

McNeil, M.A., Webster, J.M., Beaman, R.J. and Graham, T.L. (2016). New constraints on the spatial distribution and morphology of the Halimeda bioherms of the Great Barrier Reef, Australia. Coral Reefs, 35, 1343–1355.

McNeil, M.A., Nothdurft, L.D., Dyriw, N.J., Webster, J.M., Beaman, R.J. (2020). Morphotype differentiation in the Great Barrier Reef Halimeda bioherm carbonate factory: internal architecture and surface geomorphometrics. The Depositional Record 7, 176-199.

Mc Neil, M., Nothdurft, L.D., Hua, Q., Webster, J. M., Moss, P. (2022). Evolution of the inter-reef Halimeda carbonate factory in response to Holocene sea-level and environmental change in the Great Barrier Reef. Quaternary Science Reviews, 277, 107347.

Orme, G., Flood, P.G. and Sargent, G. (1978). Sedimentation trends in the lee of outer (ribbon) reefs, northern region of the Great Barrier Reef province. Philosophical Transactions of the Royal Society of London A: Mathematical, Physical and Engineering Sciences, 291, 85-99.

Phipps, C.V.G. and Roberts, H.H. (1988) Seismic characteristics and accretion history of Halimeda bioherms on Kalukalukuang Bank, eastern Java Sea (Indonesia). Coral Reefs, 6, 149–159.

Roberts, H.H., Phipps, C.V. and Effendi, L. (1987). Halimeda bioherms of the eastern Java Sea, Indonesia. Geology, 15, 371–374.

Roberts, H.H., Aharon, P. and Phipps, C.V. (1988) Morphology and sedimentology of Halimeda bioherms from the eastern Java Sea (Indonesia). Coral Reefs, 6, 161–172.

Searle, D. and Flood, P. (1988). Halimeda bioherms of the Swain reefs– southern Great Barrier Reef. Proceedings of the 6th International Coral Reef Symposium, 139–144.